A MOLECULAR DYNAMICS STUDY OF MOISTURE-INDUCED EFFECTS ON ASPHALT BINDERS AND MINERAL AGGREGATES

A Thesis

by

ELIAS I. MOUBARAK

Submitted to the Office of Graduate and Professional Studies of
Texas A&M University
in partial fulfillment of the requirements for the degree of

MASTER OF SCIENCE

Chair of Committee,	Ioannis Economou
Co-Chair of Committee,	Eyad Masad
Committee Members,	Ahmed Abdala
Head of Department,	Arul Jayaraman

December 2019

Major Subject: Chemical Engineering

ABSTRACT

The moisture effect on the work of adhesion of asphalt binder and mineral aggregates was investigated using molecular dynamic simulation. The implemented asphalt model, based on the OPLS-AA force field, was validated in terms of thermodynamic properties such as density and elastic properties (Young's modulus and Poisson's ratio). The density was about 2% below the experimental value of 1,005 kg/m^3 at ambient temperature. Two methods were used to obtain the Young's modulus: the Theodorou and Suter method and the stress-strain method. The latter one was successful in predicting a Young's modulus that is compatible with the values measured at the nanoscale (1,384 ± 595 MPa) using the Atomic Force Microscope and a Poisson's ratio of 0.4. The Theodorou and Suter method did not yield the same success. Simulation successfully demonstrated the effect of temperature on the Young's modulus, which decreased from 1,505 MPa to 1,024 MPa when temperature changed from 25 to 75°C. The Poisson's ratio was found to be constant at all temperatures.

Two mineral structures were constructed in this work, the $\{10\bar{1}4\}$ calcite and the $\{001\}$ α-quartz represented by an optimized force field and CLAYFF, respectively. Calculations were successful in predicting that at 25, 50 and 75°C and at a dry basis, the developed asphalt binder has a higher affinity to bond with calcite than quartz. It was also found that the work of adhesion for both structures was not affected by temperature. In addition, the Lennard-Jones interactions mostly contributed to the work of adhesion (80%). Calcite's work of adhesion decreased by around 41% after adding water compared

to a decrease of 21% for the case of adding water to quartz, which makes the former more susceptible to moisture damage. However, the asphalt still favored the calcite surface over quartz, which is evident by comparing the absolute values of the work of adhesion. Therefore, it is expected that the damage will start at the quartz surface before it does in the calcite surface.

DEDICATION

I would like to dedicate this work to underprivileged kids all over the world. This should be a reminder that we were given the chance to become better people and at some point, in our lives, we should give back to society.

ACKNOWLEDGEMENTS

I would like to thank my committee chair, Dr. Ioannis Economou, and co-chair, Dr. Eyad Masad, for their guidance and support throughout the course of this research.

Thanks also go to my friends, colleagues, the department faculty and staff, and the Office of Graduate Studies for making my time at Texas A&M University at Qatar a great experience.

Finally, thanks to my family and loved ones for their encouragement and patience.

CONTRIBUTORS AND FUNDING SOURCES

Contributors

This work was supervised by a thesis committee consisting of Dr. Ioannis Economou [advisor] and Dr. Ahmed Abdala of the Chemical Engineering Program at Texas A&M University at Qatar and Dr. Eyad Masad [co-advisor] of the Mechanical Engineering Program at Texas A&M University at Qatar.

Technical support was provided by Dr. Loukas Peristeras of the Molecular Thermodynamic and Modelling of Materials Laboratory at the Institute of Nanoscience and Nanotechnology, NCSR “Demokritos”, Athens, Greece.

All work conducted for the thesis was completed by the student independently.

Funding Sources

Graduate study was supported by a fellowship from Texas A&M University at Qatar.

TABLE OF CONTENTS

Page

LIST OF FIGURES

Page

LIST OF TABLES

Page

1. INTRODUCTION

In most countries, paved roads are covered with asphalt surfaces. The so-called Hot Mix Asphalts (HMAs) are obtained by liquefying the asphalt binder at elevated temperatures and mixing it with mineral aggregates.[1] Several mix design methods were developed and adopted throughout the years, based on the volumetric properties of the mixture. These mix designs are used to determine the required proportion of the binder and aggregate to ensure that the mixture meets the desired properties and achieves optimal performance, i.e. can sustain a wide range of traffic load and environmental conditions while in service.[2]

Even with the use of sophisticated mechanical tests to measure mixture properties during the design stage, pavements may still fail because of the lack of understanding of the effects of interactions at the nano- and micro-scales on macroscopic performance. Permanent deformation, also known as rutting, is one of the major distresses in pavements, which occurs because the mixture cannot withstand applied shear stresses. Rutting becomes more pronounced during hot weathers when asphalt binder loses some of its shear strength and ability to bond the mineral aggregate structure.[1] Repeated traffic load over long periods might also cause the mix to crack, which is known as fatigue damage. Similarly, in very cold regions, low temperatures are responsible for pavement cracking.[3] It is primarily linked to the properties of the asphalt binder at low temperatures. Another important distress is stripping, or moisture-induced damage. The aggregate-asphalt binder adhesive force is weakened due to the presence of moisture/water at the interface. The exact behavior depends on a variety of factors including the characteristics of both the

asphalt binder and aggregate, traffic loading, environment, and the use of additives.[1] To overcome moisture damage one can use antistripping agents. However, their use is not always effective and may result in other problems such as cracking and reduction of fatigue life.[3] Therefore, to minimize moisture damage, one needs to understand the fundamentals of aggregate-asphalt adhesion i.e. the affinity of dissimilar components or surfaces to adhere to one another due to chemical and physical forces such as covalent bonding, hydrogen bonding, polar, electrostatic and van der Waals forces.

Experimental efforts have already succeeded in quantifying moisture sensitivity of HMAs based on the different mechanical properties of the mix before and after introducing moisture into it. In an attempt to provide a more profound explanation, Bhasin et al.[4] were able to quantify moisture sensitivity experimentally by drawing a relation between the cohesive and adhesive forces of HMAs and the surface free energies of asphalt binders and aggregates. They concluded that the appropriate selection of material based on surface free energies should ensure a more resistant mix to moisture damage and reduces the effects of stripping on pavement performance.[4] However, experimental studies were not able to identify the fundamental mechanisms contributing to moisture failure of HMAs. To this respect, the use of modeling tools offers a reliable approach, complimentary and in combination to the experimental work, for improving our understanding on the fundamental aspects in the field.

Molecular Dynamics (MD) simulation is a powerful modeling technique for studying phenomena taking place in chemical, biological and physical systems at the atomistic level. MD simulations, like all relevant computational techniques, can serve as

computer experiments to generate results that can be used to test theories.[5] In some cases, especially when actual experiments are not feasible, MD simulations are the only resort to test the quality of a theory.[5] Typical results obtained from MD simulations are dynamic properties as well as fundamental thermophysical properties. In the context of our work, MD was used to investigate the binder's properties such as its density, Young's modulus, Poisson's ratio and cohesive energy density at the nano-scale. MD was also used to study the physical effect of moisture on the adhesion forces developed between asphalt binders and aggregates in a range of conditions. This thesis aims at gaining a better understanding of the properties of asphalt binders and their adhesion with mineral aggregates in the presence and absence of water by mean of molecular modeling techniques and MD in particular.

1.1. Motivation for this Work

With its growing infrastructure, which is part of the country's economic development and vision 2030, Qatar is building new roads as part of a bigger project. Qatar imports asphalt binders and aggregates for construction of asphalt pavements. The sources of these raw material vary, which causes inconsistency in material properties and less reliability of the predictions of pavement performance. In addition, Qatar is known for its hot and humid weather making the roads susceptible to moisture damage.

An MD study offers an in-depth analysis, at the atomistic level, on the compatibility between asphalt binders and mineral aggregates, based on moisture effects. It would help determine the best fit in terms of adhesion and resistance to moisture damage leading to better pavement performance.

1.2. Aim and Objectives

The aim of this thesis is to use MD simulation to investigate the effect of moisture on the adhesion of asphalt binders and aggregates. The various objectives associated with this goal are summarized below:

1. Validation of the all-atom Optimized Parameters for Liquid Simulations[6-8] (OPLS-AA) as a force field for the prediction of physical properties of a broad range of hydrocarbons (i.e., n-alkanes, aromatics, polyaromatics, etc.);
2. Development of an asphalt model based on Derek and Greenfield[9]'s proposed structures that agree with the experimental SARA fractions;
3. Construction of a fully equilibrated and relaxed system in terms of the potential energy, pressure, cohesive energy density and autocorrelation function;
4. Validation of the model against experimental properties such as density, Young's modulus and Poisson's ratio;
5. Comparison of molecular simulation results generated from this work against experimental data available in the literature;
6. Development of a molecular framework that can guide accurate design of asphalt binders and aggregates with optimum mechanical properties in real life applications.

2. LITERATURE REVIEW

2.1. Asphalt Binders

Asphalt binders are the byproduct of crude oil distillation.[1] Depending on the type of crude and the specification requirements, these asphalt binders can be either directly precipitated by vacuum fractionation or produced by solvent deasphalting, solvent extraction and continuous air blowing.[1] In general, at ambient temperatures, the asphalt binder is a black and highly viscous semisolid material.[1] Its complex structure makes it nearly impossible to identify the exact chemical formula of its components and the composition. Nevertheless, it is widely accepted that hydrocarbons, are at the core of the asphalt binder chemistry. These hydrocarbons can be grouped, based on the carbon atoms links, into aliphatic/paraffinic structures of straight or branched chains, aromatic structures of unsaturated rings, and naphthenic structures of saturated rings.[1] In addition to hydrogen and carbon, heteroatoms such as sulfur, nitrogen and oxygen are found in asphalt molecules but in small percentages and attach to carbon covalently. These heteroatoms cause an asymmetric electron distribution within a molecule creating dipole moments.[1] Due to the electrical imbalance, electropositive and electronegative polar groups emerge. The electrostatic interactions between the different polar groups along with the Van der Waal's interactions between the non-polar groups influence the physical properties of asphalt binders[1] which will eventually affect the properties of HMAs.

The simplest compositional model suggests that asphalt binders are made up of asphaltenes, resins and oils.[1] Asphaltenes, being the most complex and polar constituents

of binders, are precipitated in nonpolar solvents such as n-heptane and n-pentane. They tend to associate and form conglomerates due to their high polarity.[1] Resins on the other hand, are soluble in n-pentane. They play an important role increasing the homogeneity of the mixture by dispersing the asphaltenes.[1] Oils are usually paraffinic, saturated hydrocarbons with no heteroatoms, and are soluble in most solvents.[1] Moreover, oxidation processes cause changes in the structures of resins and oils yielding more asphaltenes.[1] Hence, the polarity of the molecules will increase causing a higher level of association in the mixture. The outcome would be a shift in the properties and performance of asphalt binders. Several analytical procedures have been developed to separate the aforementioned components of asphalt binders. However, the generic fractions/classes obtained out of these separations were still complex mixtures.[1]

A widely used procedure is the selective adsorption-desorption method developed by Corbett[10-11], which is based on solubility differences. Figure 1 demonstrates the selective adsorption-desorption procedure. First, asphaltenes are precipitated by n-heptane. Then, the n-heptane solution along with the soluble fractions are introduced into an alumina-based chromatographic column where they are adsorbed.[1] Finally, the different fractions are sequentially desorbed using solvents of increasing polarity such as n-heptane, benzene, a mixture of methanol and benzene and trichloroethylene. The procedure yields four distinct classes: Asphaltenes (A), Saturates (S), Naphthene Aromatics (NA) and Polar Aromatics (PA)/Resins (R).

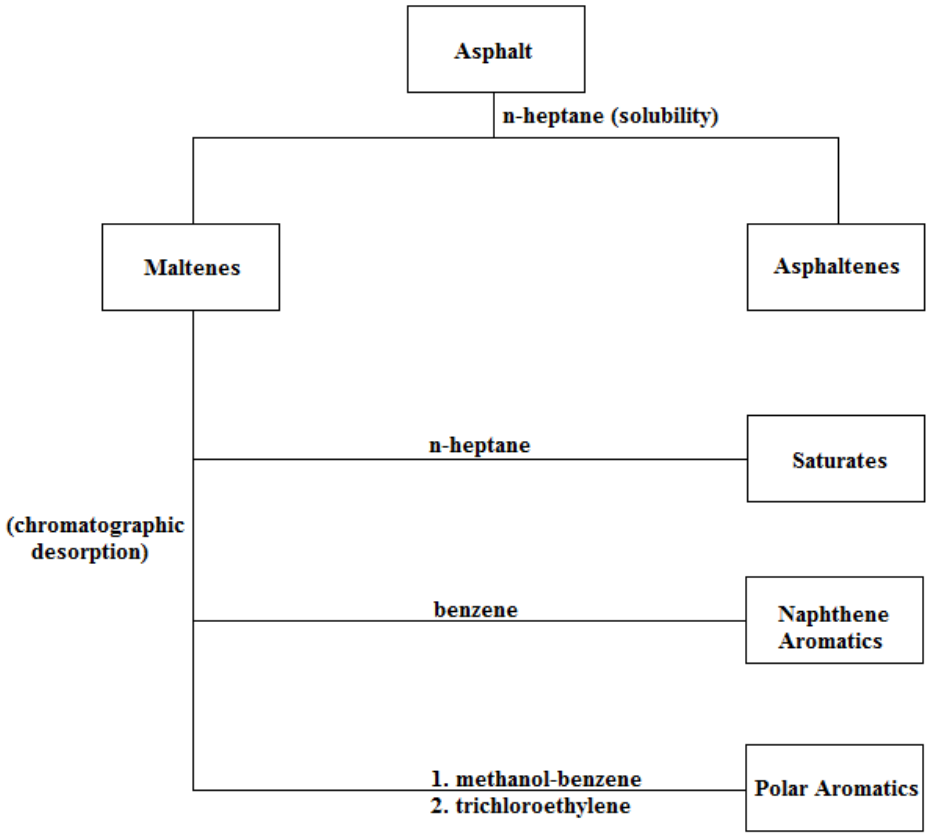

Figure 1: Selective adsorption-desorption procedure to characterize asphalt binders.[1]

The same earlier discussion holds for asphaltenes. Saturates are paraffinic compounds that might contain sulfur in some cases. Naphthene Aromatics are condensed nonaromatic and aromatic ring systems that may contain heteroatoms. Polar Aromatics resemble the naphthene aromatics but with a higher percentage of aromatic ring systems. Each class plays a major role in the physical, chemical and rheological properties of the asphalt binder.[1] Consequently, one needs to construct a realistic asphalt model in MD that predicts well these properties. To this respect, Derek and Greenfield[9] developed representative molecular models of asphalt components based on previously identified

compounds in petroleum and geochemistry studies. These components were classified into the four different generic asphalt classes based on their Hansen solubility parameters, size and functional groups.[9] The molecular structures of these components are illustrated below. The proposed structures will be at the core of the asphalt model we aim at developing.

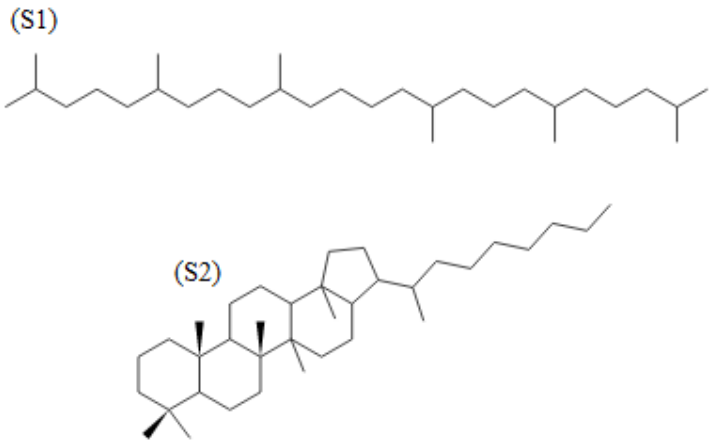

Figure 2: Saturates, (S1) - squalane (SQU) (S2) - hopane (HOP).[9]

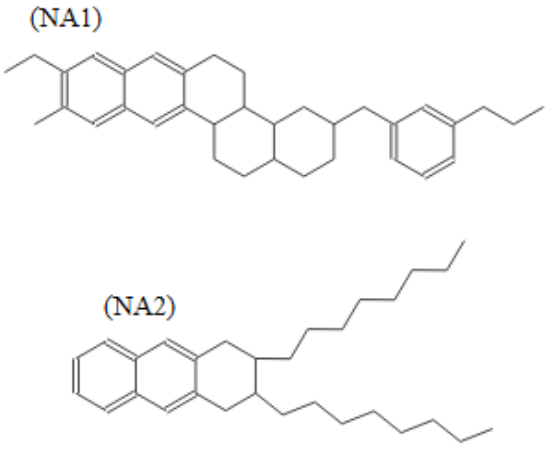

Figure 3: Naphthene Aromatics, (NA1) - perhydrophenanthrene-naphthalene (PHP) (NA2) - dioctyl-cyclohexane-naphthalene (DOC).[9]

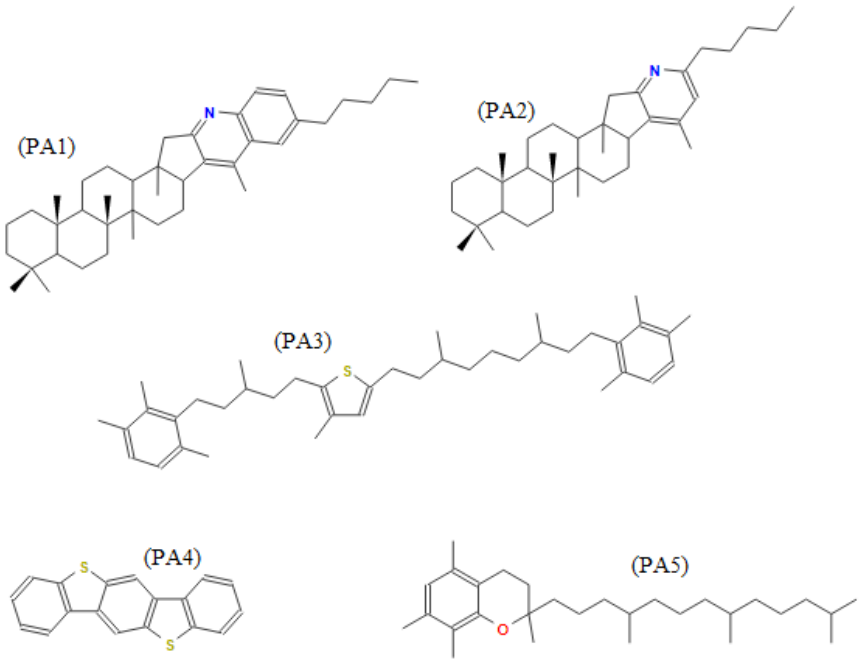

Figure 4: Polar Aromatics, (PA1) - quinolinohopane (QLH) (PA2) - pyridinohopane (PYH) (PA3) - thio-isorenieratane (TIR) (PA4) - benzobisbenzothiophene (BBT) (PA5) - trimethylbenzene-oxane (TBO).[9]

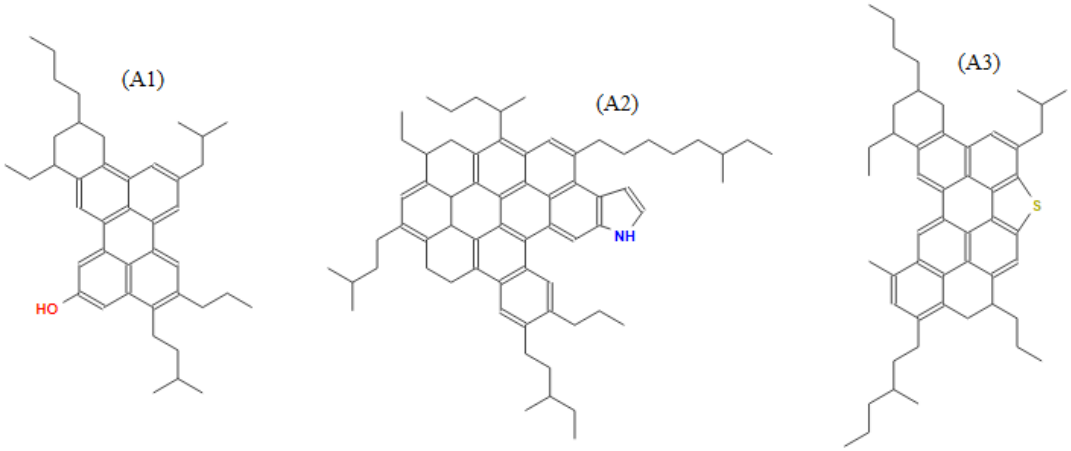

Figure 5: Asphaltenes, (A1) - asphaltene-phenol (MOA) (A2) - asphaltene-pyrrole (MOB) (A3) - asphaltene-thiophene (MOC).[9]

2.2. Aggregates

Aggregates used in road pavement are mainly obtained from naturally occurring geological formations, known as rocks. These natural rocks are classified into three groups: igneous, sedimentary and metamorphic based on their formation mechanism and origin.[1] In addition, other artificial aggregates are produced for specific applications[1], i.e. to enhance HMA performance.

The physical properties of aggregates are of high importance for road construction. Aggregates must possess specific characteristics to be suitable for use in HMA. First, aggregates are required to be hard and tough to resist crushing and degradation during production, and disintegration when in service due to traffic loads.[1] Also, they should be durable to resist the effects of weathering and aging.[1] In addition, aggregates should be properly graded and consist of cubical particles with low porosity to attain higher internal friction resulting in higher mechanical stability.[1] Moreover, the cleaner and rougher the surface of the aggregates the better. They will form stronger bonds with asphalt binders.[1] Finally, aggregates must have hydrophobic surfaces to repel water and prevent moisture damage and stripping.[1]

The chemical properties of aggregates such as wetting, adhesion and stripping are mainly affected by the mineral's composition and structure.[12] Most aggregates include a combination of minerals such as quartz, plagioclase, muscovite, calcite, dolomite, illites and others.[12] These minerals play a decisive role in the adhesion of asphalt binders and aggregates.[12] Therefore, determining the mineral composition of aggregates helps identifying the HMA's stripping resistance. In 2013, Al-Ansary and Iyengar[13] published

a study on the physicochemical properties of aggregates used in construction activities in Qatar. In this thesis, we focus on local limestone; the quantitative analysis of which shows that it comprises of 34.15% calcite ($CaCO_3$), 10.77 % quartz (SiO_2) and 55.08% dolomite ($CaMg(CO_3)_2$).[13] The stripping resistance of each mineral is different as each of them has a different susceptibility to moisture. Nevertheless, damage will start at the weakest link.

2.3. MD Studies of Asphalts

Asphalt systems have been widely studied by means of MD simulations during recent years. In 2007, and after developing the first set of representative asphalt molecular models, Zhang and Greenfield[14] studied the glass transition behavior by analyzing thermodynamic properties such as density, isothermal compressibility and thermal expansion coefficient of modeled asphalts. They also studied the orientation of asphalt molecules within the mixture with respect to temperature and distance between neighboring molecules.[15] They modeled the asphalt as a three-component mixture. N-docosane and 1,7-dimethylnaphthalene represented the saturates and naphthene aromatics respectively. The asphaltenes were represented by either one of the two molecules previously studied in published literature.[14] These different molecules are shown in Figure 6. The OPLS-AA forcefield was used to represent the atomic structures explicitly. A combination of Metropolis Monte Carlo (MC) and MD simulations was implemented to estimate the properties of interest. It was suggested that the glass-transition temperature (T_g) lies between 25 and 85°C.[14] In addition, the two asphaltenes were found to orient themselves differently with respect to temperature. At low temperatures, asphaltene1

molecules were almost parallel, whereas asphaltene2 molecules were packed in a T-shaped orientation. At higher temperatures, the opposite was true.[15]

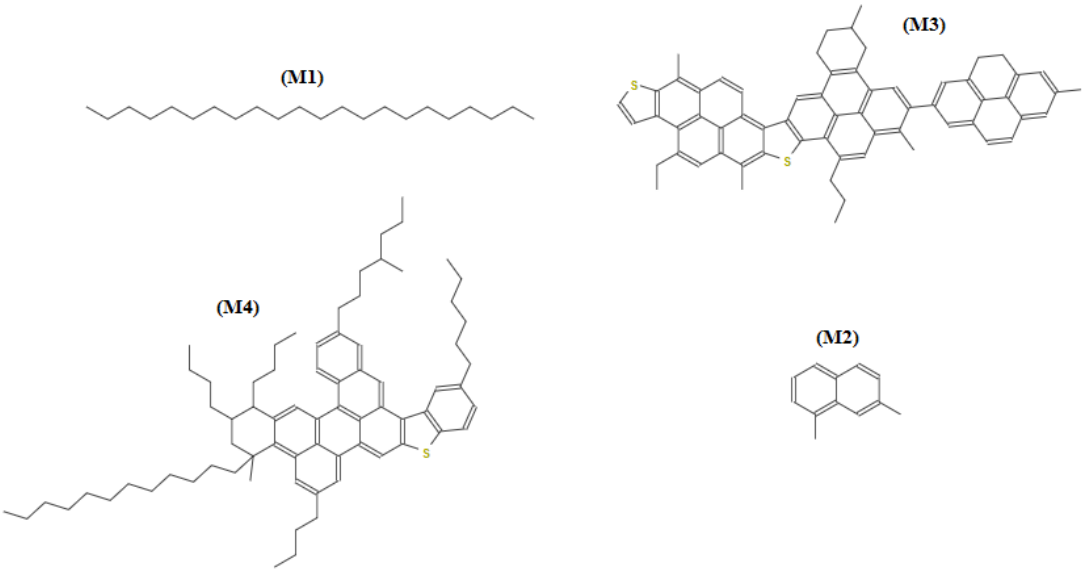

Figure 6: Three-component asphalt model. (M1) - n-docosane (M2) - 1,7-dimethylnaphthalene (M3) - asphaltene1 (M4) - asphaltene2.[14]

Four years later, Tarefder and Arisa[16] determined the change in density and glass-transition temperature of asphaltenes and resins due to aging. In their study, they used a modified version of the asphaltene2 molecule developed by Zhang and Greenfield[14] and two resin molecules taken from Venezuelan crude oil. The different molecules are displayed in Figure 7. The DREIDING forcefield was used to represent the atomic structures. The results showed that at oxidation levels higher than 20%, the T_g falls below -5°C for asphaltenes. For resins, the study was inconclusive as the relation between the oxidation level and the T_g couldn't be generalized.[16] Following his studies of the effect of aging on density and transitional temperature, Tarefder, along with Pan[17], investigated the

changes in intermolecular interactions, density, bulk modulus and zero shear viscosity of model asphalt systems due to oxidation.

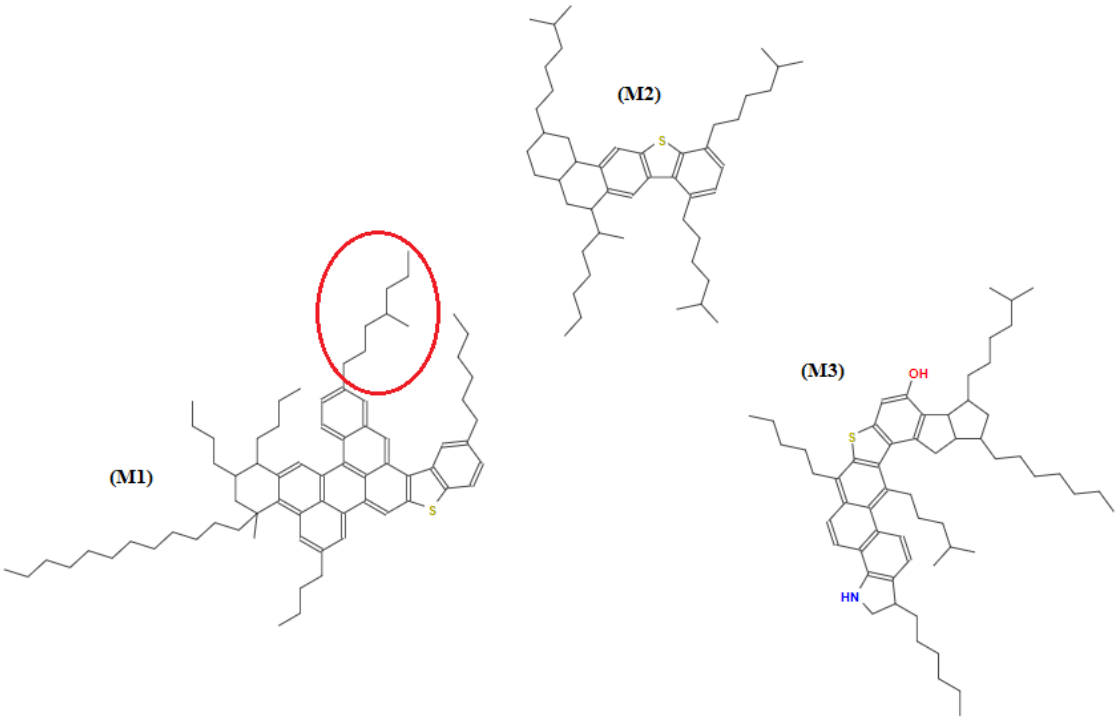

Figure 7: Tarefder's molecular models. (M1) - modified asphaltene2 (chain encircled in red was removed) (M2) - resin1 (M3) - resin2.[16]

They used the asphalt model developed by Derek and Greenfield as a basis[9] and implemented the DREIDING forcefield. Then, they added carbonyl groups to account for the oxidative changes in the chemical structure of all the molecules. It turned out that oxidized asphalt has a higher bulk modulus, density and viscosity than virgin asphalt. Therefore, virgin asphalt deformed faster and more than the oxidized asphalt under different stress rates. In addition, both types of asphalt, virgin and aged, were more susceptible to failure under tensile stresses than under compressive stresses.[17]

Wang et al.[18], in 2015, were the first to investigate the interactions of the four classes of asphalts identified by Corbett. They used some of the molecules from the Derek and Greenfield[9] model and added new molecules in an attempt to provide a better representation of the binders at hand. They implemented the Condensed-phase Optimized Molecular Potentials for Atomistic Simulation Studies (COMPASS) forcefield in a combination of MC and MD simulations. They concluded that asphaltenes must be at the core to form bee-like structures and saturates must provide a good dispersion medium.[18]

Two years later, Guo et al.[19], in 2017, studied the diffusion of the four classes of asphalt components in mineral aggregate surfaces. They focused on five main mineral components: SiO_2, Al_2O_3, CaO, MgO and Fe_2O_3. The forcefield parameters were obtained by implementing COMPASS. The team found that the diffusion speed increases with increasing molecular weight. This is true when the interfacial interaction between asphalts and aggregates is weak. The fastest average diffusion was recorded for Al_2O_3. Diffusion is further increased for all components with increasing temperature and CaO showed the highest temperature sensitivity.[19]

In 2016, Sun et al.[20] assessed the glass-transition temperature and densities of asphalt binders in an attempt to understand the self-healing performance of these binders. For that purpose, they used the three-component asphalt model developed by Zhang and Greenfield[14] along with the COMPASS forcefield. The study concluded that the modified asphalt binder showed a higher potential for self-healing due to the presence of additives.[20]

In 2017, Xu and Wang[21] studied the oxidative aging effect on asphalt binder properties such as density, surface energy, viscosity, and cohesive energy density using

the 12-component system developed by Derek and Greenfield[9]. COMPASSII, which is an extension to the COMPASS forcefield, was implemented in this study. It was found that oxidative aging introduces changes to the asphalt properties. It increases the density, cohesive energy and viscosity but reduces surface free energy. It also weakens the ability of asphaltenes to aggregate. In addition, aging causes less resistance to moisture damage.[21]

In 2016, Yao et al.[22] studied the physicochemical properties of asphalt such as density, glass transition temperature, bulk modulus and viscosity using a three-component asphalt model. In this study, the Amber Cornell Extension Force Field was implemented. The forcefield was obtained by inserting the General Amber Force Field (GAFF) parameters into the Amber Cornell Force Field. The results showed that this force field offers improved results compared to OPLS-AA used by Zhang and Greenfield[14].[22]

To this point, researchers were interested in studying the physical and chemical properties of asphalt binders. Xu and Wang[23] were the first, in 2016, to investigate the cohesion and adhesion properties of asphalt concrete with calcite and quartz by calculating the cohesive energy density and surface free energy. In this second paper, they revert to the use of the three-component asphalt model[14] but kept on implementing COMPASSII. It was shown that the cohesive energy of asphalt binders is mostly affected by Van der Waals forces. Moreover, the adhesion between asphalts and aggregates depends on the type of aggregate mineral.[23] In a later attempt, in 2017, Wang et al.[24] studied the asphalt-aggregate interface adhesion strength with moisture effects by also using the same asphalt model. However, a different forcefield was implemented this time: Consistent Valence Force Field (CVFF).

It was concluded that moisture significantly decreases the adhesion between the asphalt binder and quartz. At higher temperatures, the adhesion strength decreases, irrespective of water content. Though, beyond a certain water loading, the adhesion reaches a plateau.[24]

In most of the computational work done on asphalt systems, researchers used a three-component model that underrepresents and oversimplifies the asphalt binder actual structure. Their main focus was to obtain thermodynamic and elastic properties such as density, glass transition temperature, cohesive energy density, elastic modulus and bulk modulus for virgin and aged asphalts. These studies did not offer fundamental clarifications on the effects of interactions at the nano- and micro-scales on macroscopic performance. Hence, the understanding of distresses still relies on experimental efforts. In this work, we will:

1. Use an improved asphalt model that consists of 12 components;
2. Offer a robust protocol to equilibrate and relax asphalt structures;
3. Use thermodynamic and elastic properties such as density, cohesive energy density, Young's modulus and Poisson's ratio as means to validate the asphalt model, not as the final outcome of the research;
4. Answer fundamental questions on the effects of moisture on the adhesion between asphalt binders and mineral aggregates at the atomistic level in an attempt to minimize stripping.

3. METHODOLOGY

"A journey of a thousand miles begins with a single step". After completing the literature review in the previous section, a number of calculation protocols and workflows that were used in order to achieve the objectives set for this thesis are outlined here.

3.1. Force Field

In this section, the various force fields examined in this thesis are presented. The corresponding non-bonded and bonded parameters are provided in Appendix A.

OPLS-AA is a general force field developed mainly for proteins and provides an explicit atom description.[6] Bonds can stretch, bond angles can bend and dihedral angles are able to rotate. In this force field, the bond stretching and bond angle bending parameters were taken from the Assisted Model Building with Energy Refinement all-atom (AMBER) force field.[6] Nonbonded parameters were fitted to reproduce the heat of vaporization and the density for a group of pure organic liquids.[6] The torsional parameters were derived from ab initio calculations for around 50 organic molecules and ions.[6] The functional forms describing the energy modes of the force field are discussed below.

The Coulomb and Lennard-Jones 12-6 terms represent the non-bonded intra- and inter-molecular interactions between molecules A and B as shown in eq. 1:

$$E_{AB} = \sum_i \sum_j [\frac{q_i q_j e^2}{r_{ij}} + 4\epsilon_{ij}\left(\frac{\sigma_{ij}^{12}}{r_{ij}^{12}} - \frac{\sigma_{ij}^{6}}{r_{ij}^{6}}\right)]f_{ij} \qquad (1)$$

where i and j represent atoms in A and B respectively, q is the atomic charge and e is the elementary charge of a proton. The distance between two atoms is represented by r, ϵ is the well depth and measure how strongly two atoms attract, σ is the distance at which the

intermolecular potential between two atoms is zero and f is a dimensionless scaling factor. It is always set to 1 except for 1,4-intramolecular interactions where it takes the value of 0.5.[6] The geometric combining rules, eq. 2, are used to obtain interatomic σ and ϵ values.[6]

$$\sigma_{ij} = \sqrt{\sigma_i \sigma_j}\,; \epsilon_{ij} = \sqrt{\epsilon_i \epsilon_j} \tag{2}$$

The bond stretching and angle-bending potential energy, $E_{bond}\ and\ E_{angle}$ respectively, are shown in eqs. 3 and 4:

$$E_{bond} = \sum_{bonds} K_r (r - r_{eq})^2 \tag{3}$$

$$E_{angle} = \sum_{angles} K_\theta (\theta - \theta_{eq})^2 \tag{4}$$

where K_r and K_θ characterize the bond length and angle stiffness respectively, r_{eq} is the equilibrium bond length and θ_{eq} is the equilibrium bond angle.[6]

Finally, the torsional energy is represented by eq. 5:

$$E_{torsion} = \sum_{torsion\ angles} \frac{V_1}{2}[1 + \cos(\varphi + f_1)] + \frac{V_2}{2}[1 - \cos(2\varphi + f_2)] + \frac{V_3}{2}[1 + \cos(\varphi + f_3)] \tag{5}$$

where φ is the torsional angle, $V_1, V_2\ and\ V_3$ are the coefficients in the Fourier series and $f_1, f_2\ and\ f_3$ are phase angles.[6]

On the other hand, Transferable Potentials for Phase Equilibria - United Atoms (TraPPE-UA)[25-31] is a specific force field parametrized to cover a number of molecules at a time and provides an implicit atomistic description.[25] In all its versions, bonds are not free to stretch; hence, bond lengths are fixed.[25] However, angles are allowed to bend and

rotate.[25] The angle bending energetics are represented by eq. 6, which is similar to eq. 5 in the case of OPLS-AA:

$$E_{bend} = \sum_{angles} 0.5K_{\theta}(\theta - \theta_{eq})^2 \tag{6}$$

Nonbonded interactions are usually represented by the Lennard-Jones 12-6 potential because the united atoms in our case have a zero charge as shown in eq. 7:

$$E_{AB} = \sum_{i}\sum_{j} 4\epsilon_{ij}\left(\frac{\sigma_{ij}^{12}}{r_{ij}^{12}} - \frac{\sigma_{ij}^{6}}{r_{ij}^{6}}\right) \tag{7}$$

The Lorentz-Berthelot combining rule, eq. 8, is used to obtain interatomic σ and ϵ values.[26]

$$\sigma_{ij} = 0.5(\sigma_i + \sigma_j)\,;\epsilon_{ij} = \sqrt{\epsilon_i \epsilon_j} \tag{8}$$

The torsional potential takes different forms, depending on the type of molecules it is representing. Eq. 9 illustrates the torsional potential function for branched alkanes.[26]

$$E_{torsion} = \sum_{torsion\ angles} c_0 + c_1[1 + \cos(\varphi)] + c_2[1 - \cos(2\varphi)] + c_3[1 + \cos(3\varphi)] \tag{9}$$

where φ is the torsional angle and c_i is the coefficient in the Fourier series.[26]

In this work, to validate the use of either force fields, one is interested in the density of the asphalt binder building blocks: n-pentane, n-dodecane, 2-methylpentane, cyclopentane, cyclohexane, benzene, naphthalene, oxane, phenol, pyrrole, pyridine and thiophene, in addition to the dihedral angle distributions and radial distribution functions. These molecules were chosen because they form molecular asphalt structures.

In the case of OPLS-AA, the aforementioned molecular structures were constructed using the LigParGen web server[32], which was developed to provide OPLS-AA force field parameters for organic molecules using different CM1A charge models. The CM1A charge model developed by Cramer et al.[33-38] is based on detailed quantum mechanical calculations and is compatible with OPLS-AA. The force field parameters were assigned by applying the 1.14*CM1A-LBCC model, which offers an improved charge distribution over the 1.14*CM1A by applying localized bond charge corrections.[39]

In the case of TraPPE-UA, bond lengths and angles were used to draw initial 2-D structures for nonplanar molecules as shown in Figure 8. The first atom is fixed at the origin. Then, the coordinates of all other atoms are obtained by applying Pythagoras theorem. For planar molecules such as benzene[27], the virtual site approach was implemented to restrain all atoms to fixed positions. First, the moment of inertia of the ring shown in Figure 9 was calculated.

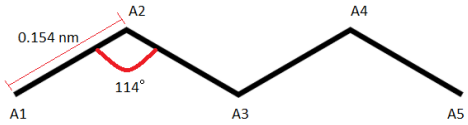

Figure 8: Skeletal structure of pentane

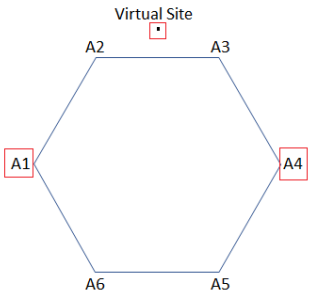

Figure 9: A scheme illustrating the virtual site approach for benzene

Second, atoms A1 and A4 were taken as the reference and the mass of the group of atoms A2, A3, A5 and A6 was calculated. Then, the virtual site having the same mass as the group of atoms was inserted such that to preserve the inertia of the ring. Finally, atoms A2, A3, A5 and A6 were projected into the plane formed by the basis and the virtual site. The force field parameters were obtained from the literature[26, 40].

At this point, the task was to equilibrate and relax the created structures. A general protocol was developed and applied:

1. Initially, cubic cells of low density were built in 3-D periodic boundary conditions
2. A 2 nanosecond (ns) isotropic[41] NPT simulation at the required conditions of temperature and pressure was carried out for each structure
3. The density was calculated from the last 0.5 ns, after the systems had reached equilibrium in terms of potential energy and density

For both force fields, the leapfrog algorithm[41] was used to integrate the Newton's equations of motion. A time constant of 1 femtosecond (fs) was assigned. The temperature and pressure were coupled with the Berendsen thermostat[41] and Berendsen barostat[41] respectively with a time constant of 1 picosecond (ps). The compressibility of the system was imposed at 0.00009 bar^{-1}. The energy and pressure corrections[41] were implemented to account for the changes in the system taking place beyond the cut-off. The cut-off radius was set at 1.5 nanometer (nm) for OPLS-AA and 1.4 nm for TraPPE-UA for the van der Waals and the Coulombic interactions. The Particle Mesh Ewald (PME)[41] was used to describe the electrostatic interactions for OPLS-AA; whereas, the cut-off scheme[41] was used to describe the Coulombic interactions for TraPPE-UA.

3.2. Asphalt Molecular Structure

In this research, 11 out of the 12 proposed molecular structures shown in Figure 2-Figure 5 were constructed using the LigParGen server. The asphaltene-pyrrole was an exception to the automated assignment due to the limitation of the server implementation that supports no more than nine fused rings in the molecular structure. In this case, the bonded and nonbonded parameters were deduced from similar structures: asphaltene-phenol, asphaltene-thiophene and pyridine; while the charges derived by Derek and Greenfield[9] were implemented. The generated molecular structures were used to develop two different asphalt models, AS1 and AS2, based on the experimental SARA analysis of a low-density asphalt binder (WL)[42] used for road pavement in Qatar. The SARA analysis is shown in Table 1.

Table 1: SARA experimental analysis of WL asphalt binder[42]

Class	Saturates	Aromatics	Resins	Asphaltenes
$SARA_{exp}$ wt. %	27.43	50.36	12.42	9.80

To create the models, one needs to specify their composition, i.e. the number of constituent molecules from each class. First, the contribution of a pure component's molecular weight to the class average molecular weight ($\overline{MW_i}$) was defined by specifying the fractions ($x_{i,j}$) of pure components within each class (eq. 10). Second, the total mass of the model was obtained from the experimental density of WL and the desired final volume of the simulation box (eq. 11). The final volume was obtained after creating and equilibrating a test model. Third, using the SARA experimental fractions for each class ($SARA_i$), the corresponding masses, m_i were calculated (eq. 12). Then, based on $\overline{MW_i}$

and m_i, the total number of molecules within each class, N_i was specified (eq. 13). Finally, the number of molecules of the pure component was calculated based on their fractions ($x_{i,j}$) and the number of molecules (N_i) of the corresponding class (eq. 14). The listed general steps are summarized by the equations below.

Step 1 $$\overline{MW_i} = \sum_{j=1}^{k} x_{i,j} MW_{i,j} \quad (10)$$

Step 2 $$m_{total} = \rho_{exp} \times V_{final} \quad (11)$$

Step 3 $$m_i = SARA_i \times m_{total} \quad (12)$$

Step 4 $$N_i = (m_i / \overline{MW_i}) \times N_A \times 1000 \quad (13)$$

Step 5 $$N_{i,j} = x_{i,j} N_i \quad (14)$$

where subscript j indicates the type of molecule, the subscript i indicates the class, k indicates the number of molecules in a class, $SARA_i$ indicates the experimental class weight fraction, $\rho_{exp} = 1005 \frac{kg}{m^3}$, N_A is Avogadro's number and $V_{final} = 2.16 \times 10^{-25}\ m^3$ being the expected final volume of the simulation box at 25°C.

3.3. Simulation Methods

In this work, MD and Metropolis MC molecular simulation techniques were applied to evaluate the systems' behavior and measure the targeted properties. All MD simulations were performed using the 2016 version of GROningen Machine for Chemical Simulations (GROMACS)[41]. The MC simulations were accomplished by using the Monte Carlo for Complex Chemical Systems (MCCCS) Towhee code[43].

3.3.1. Structure Equilibration

The initial task was to equilibrate and relax the created structures. It is crucial to have a well-equilibrated system in terms of density, potential energy and pressure. A specific and robust protocol was developed and applied:

1. Initially, cubic cells of low density were built applying 3-D periodic conditions. Eight different configurations of each cell were randomly generated by means of the "gmx insert-molecules"[41] GROMACS functionality;
2. A 25 ns isotropic NPT simulation at 25°C was carried on for each configuration maintaining the shape of the cell, while equilibrating the density;
3. The isotropic NPT simulation was followed by an annealing process. The temperature was raised gradually by increments of 25°C from 25 to 150°C, then by increments of 100°C from 150°C to 950°C and then brought back the same way;
4. The different configurations underwent another 25 ns NPT simulation at 25, 50, 75, 100, 125 and 150°C. However, in this case, anisotropic barostating[41] was applied, where the three box dimensions were decoupled resulting in orthorhombic simulation cells.

In the second, third and fourth steps, the velocity Verlet scheme algorithm[41] was applied along with a time step of 1 fs. The cut-of radius was set at 1.5 nanometer (nm) for the van der Waals and the Coulombic interactions. The Particle Mesh Ewald (PME) was used to describe the electrostatic interactions. The temperature and pressure were coupled with the v-rescale thermostat[41] and Berendsen barostat respectively with a time constant

of 1 ps. The compressibility of the system was imposed at 0.00009 bar^{-1}. Finally, the energy and pressure corrections were implemented.

3.3.2. Cohesive Energy Density Calculations

The cohesive energy density is defined as "the energy required to break all intermolecular physical links in a unit volume of the material"[44]. In order to calculate the cohesive energy density for each structure, the Lennard-Jones and electrostatic contributions per molecule were added and then divided by the volume. Calculations were repeated for all configurations to obtain the average cohesive energy density at each temperature.

3.3.3. Mechanical Property Calculations

The next step is to calculate the Young's modulus (E) and the Poisson ratio of the system at 25, 50 and 75°C. The former is a measure of the strength of interatomic forces of materials and it describes its relative stiffness.[45] While the latter is defined as "the ratio of transverse contraction (or expansion) strain to longitudinal extension strain in the direction of stretching force"[46]. At a specific temperature and for a given configuration, these mechanical properties can be obtained by either applying the Theodorou and Suter method or conducting the stress-strain simulation method.

1. The Theodorou and Suter[47] method is applied usually for glassy structures satisfying the requirements of mechanical equilibrium. The entropic contributions to the mechanical properties are neglected compared to the potential energy effects.[48] In this method, one starts by applying a uniform hydrostatic compression (in 3-D) followed by uniaxial tension in each direction (x, y and z). The degree of

deformation is limited to 1% change by volume. Therefore, the applied deformations range from -1% to 1% by an increment of 0.1%. After each deformation, the local potential energy is minimized and recorded. Two algorithms are used sequentially to minimize the energy: the steepest descent[41] with 5,000 steps and a tolerance of 10^{-1} followed by the conjugate gradient[41] with 100,000 steps and a tolerance of 10^{-4}. It follows that for the hydrostatic compression and the uniaxial tension in the three directions (x, y and z); the average minimized potential energy over the eight configurations is fitted to a second-degree polynomial in the volume fractional change (ε) as shown in eqs. 15 and 16. In both equations, the first term represents the initial potential energy of the non-deformed system, whereas the second and third terms represent the internal pressure and deformation contribution to the potential energy respectively. Using these equations, one can compute the lamé constants (μ and λ) and deduce the elastic modulus (E) and Poisson ratio (ν) from eqs. 17 and 18 respectively, where:

For hydrostatic compression, the expression of the potential energy is as follows

$$U = U_0 - V_0\left(-P + \frac{\alpha_p T}{\kappa_T}\right)_0 \varepsilon + \frac{1}{2}V_0\left(\frac{2}{3}\mu + \lambda\right)\varepsilon^2 \qquad (15)$$

For uniaxial tension, the expression of the potential energy is as follows

$$U = U_0 + V_0(\tau_{11} + \rho_0 c_E T\gamma_{11})\varepsilon + \frac{1}{2}V_0(2\mu + \lambda)\varepsilon^2 \qquad (16)$$

The elastic modulus and Poisson ratio are expressed as follows

$$E = \mu \frac{3\lambda + 2\mu}{\lambda + \mu} \tag{17}$$

$$\nu = \frac{\lambda}{2(\lambda + \mu)} \tag{18}$$

2. In the Stress-Strain method[22], a continuous uniaxial tension in the x-direction with a deformation of 2.5% for the eight configurations is initiated. Then, the stress (σ) - which is the pressure of the system in the specified direction - is plotted versus the strain (ε_x), which is the fractional elongation in the main axis. Then curves are smoothened by applying the adjacent-averaging over 500 points. Finally, the smoothed curves are averaged, and the elastic modulus is obtained by linearly fitting the smoothed average:

$$\sigma = E \tag{19}$$

In order to calculate the Poisson ratio, the side length is plotted against time for the y and z directions. The plots are smoothened by applying the adjacent-averaging over 50 points. Then, the Poisson ratio in each direction and for all the configurations is calculated by applying the following formula:

$$\nu_{y,z} = -\varepsilon_{y,z}/\varepsilon_x \tag{20}$$

where the strain ($\varepsilon_{x,y,z}$) is obtained by subtracting the final length from the initial one using the smoothened values. Finally, the average Poisson ratio is computed by averaging over all configurations and over all directions. This protocol is repeated in the other two directions to obtain the elastic modulus and the Poisson ratio. In conducting the stress-strain experiment, the temperature and pressure of

the system were coupled with the Nose-Hoover thermostat[41] and Parrinello Rahman barostat[41] respectively.

3.3.4. Moisture Effect on Adhesion

The final step is to study the effect of moisture on the adhesion between the asphalt binder and the different minerals, calcite and quartz. "The work of adhesion is defined as the free energy changes or reversible work done, to separate unit areas of two different surfaces from contact to infinity".[49] Three force fields, Xiao et. al.[50], CLAYFF[51] and TIP3P[52], were used to represent calcite, quartz and water respectively.

A new transferable force field was developed by Xiao et. al.[50] to study the physical and mechanical properties of organic-inorganic complex systems. The force field was primarily developed for aragonite. However, it could be successfully transferred and implemented with other $CaCO_3$ polymorphs.[50] In their approach, they decided to use the Lennard-Jones 12-6 potentials to describe the van der Waals interactions rather than the Buckingham potentials. The C-O bonds were constrained and were not allowed to stretch. However, the O-C-O angles were free to bend and rotate in the plane. The overall potential function of the developed force field is shown in eq. 21:

$$V_{total} = \sum_i \sum_j \left[\frac{q_i q_j e^2}{r_{ij}} + \left(\frac{c^{(12)}}{r_{ij}^{12}} - \frac{c^{(6)}}{r_{ij}^{6}}\right)\right] + \sum_{angle} \frac{1}{2} K_\theta (\theta - 120) + \sum_{plane} K_\varphi (1 - \cos(2\varphi)) \quad (21)$$

where i and j represent the atoms in the calcite structure, q is the atomic charge and e is the elementary charge of a proton. The distance between two atoms is represented by r,

$c^{(12)}\ and\ c^{(6)}$ are the Lennard-Jones parameter. The angle and torsion energy terms are K_θ and K_φ respectively, with $\theta\ and\ \varphi$ being the bend and torsion angles respectively. The geometric combining rules, eq. 22, are used to obtain interatomic Lennard-Jones parameters.[50]

$$c_{ij}^{(12)} = \sqrt{c_i^{(12)} c_j^{(12)}}\ ; c_{ij}^{(6)} = \sqrt{c_i^{(6)} c_j^{(6)}} \tag{22}$$

The water-mineral Lennard-Jones cross-terms where derived by utilizing the TIP3P[52] water model and the monohydrocalcite structure. Whereas, the protein-mineral cross-terms can be obtained by applying the geometric combination rules between OPLS-AA and the newly developed force field atomwise parameters.[50]

CLAYFF[51] is a general force field developed mainly for simulating hydrated and multicomponent mineral systems such as α-quartz with aqueous solutions. Interatomic Lennard-Jones 12-6 potential parameters for metal-oxygen interactions were optimized using spectroscopic and crystallographic data of different hydrated compounds.[51] The O-O and O-H interaction potentials were derived from the SPC[53] flexible water model.[51] The electrostatic interactions are described by the Coulombic energy in eq. 23. The van der Waals interactions are described by the Lennard-Jones 12-6 potential (eq. 24).

$$E_{coulomb} = \sum_i \sum_j \frac{q_i q_j e^2}{r_{ij}} \tag{23}$$

$$E_{VDW} = \sum_i \sum_j D_{0,ij} \left(\frac{R_{0,ij}^{12}}{r_{ij}^{12}} - 2 \frac{R_{0,ij}^{6}}{r_{ij}^{6}} \right) \tag{24}$$

where i and j represent the atoms in the quartz structure, q is the atomic charge and e is the elementary charge of a proton. The distance between two atoms is represented by r, D_0 and R_0 are the empirical parameters derived from the fittings. The Lorentz-Berthelot combining rule, eq. 25, is used to obtain interatomic values.[51] The interactions of the quartz with and with asphalt molecules are derived by using the geometric combining rule.

$$R_{0,ij} = 0.5(R_{0,i} + R_{0,j})\,; D_{0,ij} = \sqrt{D_{0,i}D_{0,j}} \tag{25}$$

Hydroxyl bonds are free to stretch, just like in the SPC water model. The stretch energy is described by simple harmonics in eq. 3. An improvement of the CLAYFF force field is that it incorporates an angle bending term that considers the metal-oxygen-hydrogen vibrations. The bend energy is described in eq. 4.

Liquid water at ambient conditions will be described by the TIP3P[52] force field. The rigid water monomer is represented by three interaction sites, one oxygen and two hydrogens bearing negative and positive charges respectively.[52] The TIP3P was obtained by improving the energy and density of liquid water for the TIPS model. Water molecules in this model are rigid. Therefore, the potential function for the TIP3P water model involves only Lennard-Jones and Coulombic interactions as shown in eq. 26.

$$E_{AB} = \sum_i \sum_j \left[\frac{q_i q_j e^2}{r_{ij}} + \left(\frac{c^{(12)}}{r_{OO}^{12}} - \frac{c^{(6)}}{r_{OO}^{6}}\right)\right] \tag{26}$$

where i and j represent the atoms in the quartz structure, q is the atomic charge and e is the elementary charge of a proton, r_{OO} is the equilibrium distance between the oxygen atoms of water molecules A and B and $c^{(12)}$ and $c^{(6)}$ are the Lennard-Jones parameters.

The approach for calculating the adhesion energy is as follows:

1. The mineral structures were generated by forming the bulk and then cleaving the corresponding surface. Asphalt structures were built as orthorhombic cells having different x, y and z dimensions as their corresponding minerals;
2. These asphalt structures were equilibrated by applying steps 2 and 3 in the structure equilibration section. However, the system was allowed to move in the z- direction only keeping the x and y dimensions constant;
3. The complex asphalt-mineral system was put together and further relaxed by applying a 15 ns NPT simulation. This time, the system underwent a semiisotropic pressure coupling[41], where the x and y directions were coupled together and decoupled from the z-direction;
4. The work of adhesion was calculated on a dry basis at 25, 50 and 75°C, using the Lennard-Jones and electrostatic interactions;
5. The chemical potential of water, in the bulk, was calculated at 25°C using a Grand Canonical Monte Carlo (GCMC) simulation. Then this chemical potential was used to predict the water loading of each complex structure;
6. The water is added to the complex system that would undergo a 5 ns NPT to further relax and distribute the water molecules;
7. The work of adhesion on a wet basis was finally calculated at 25, 50 and 75°C.

4. RESULTS AND DISCUSSION

4.1. Force Field Validation

4.1.1. Density

The asphalt binder building blocks can be grouped into linear and branched alkanes (n-pentane, n-dodecane and 2-methylpentane) cycloalkanes (cyclopentane and cyclohexane), benzene, naphthalene and hetero-molecules (oxane, phenol, pyrrole, pyridine and thiophene). Four different conditions of temperature and pressure were chosen to be simulated for each component based on the available experimental data found in the literature. Figure 10 illustrates the initial and final structures of n-dodecane at 25°C.

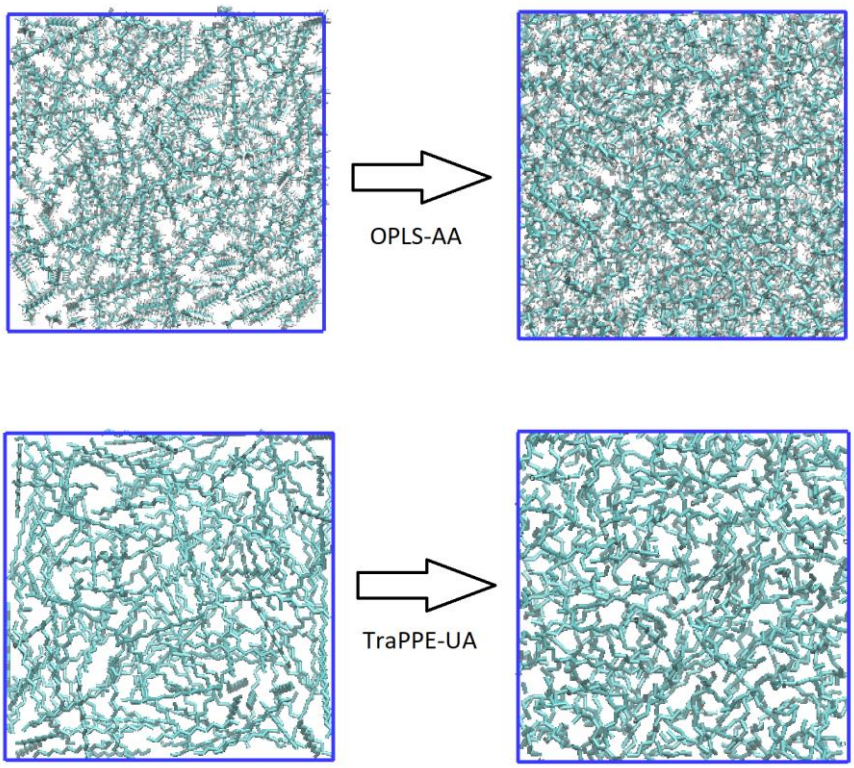

Figure 10: Equilibration process of n-dodecane at 25°C

Simulations were conducted for all components using OPLS-AA. However, only seven molecules were simulated using TraPPE-UA: n-pentane, 2-methylpentane, n-dodecane, cyclopentane, cyclohexane, benzene and oxane. For the rest of the components, the density was obtained from other simulation work in the literature. Figures 11 and 12 illustrate the calculated density of 2-methylpentane and benzene respectively using OPLS-AA and TraPPE-UA in comparison to experimental data. Refer to Appendix B for the complete set of conditions and results.

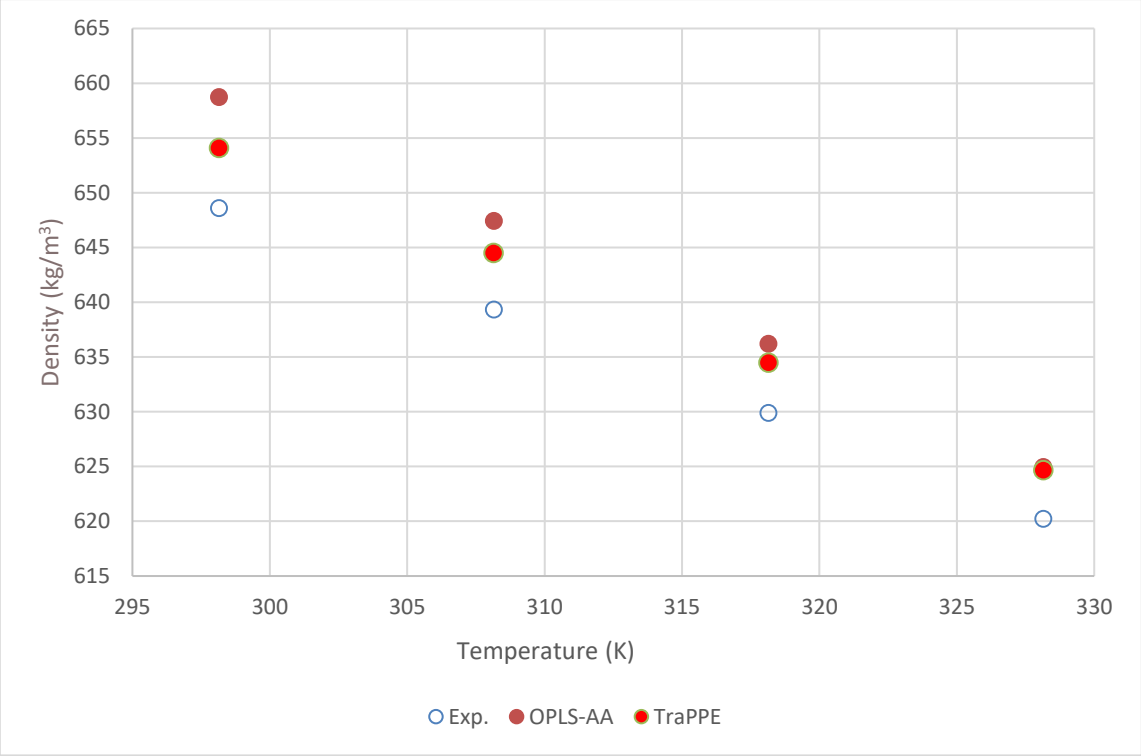

Figure 11: Density of 2-methylpentane using OPLS-AA and TraPPE-UA

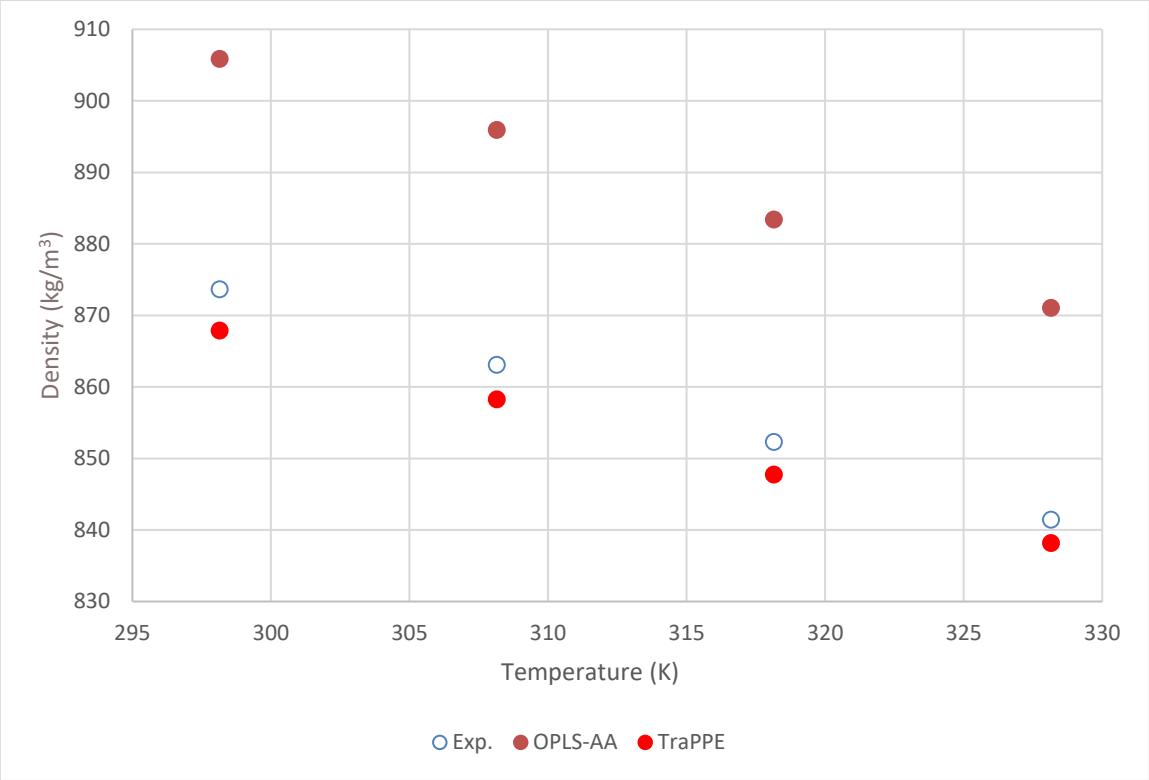

Figure 12: Density of benzene using OPLS-AA and TraPPE-UA

From the overall set of results in Appendix A, one can observe the following:

1. The density of linear and branched alkanes is within 2% of the experimental density for both OPLS-AA and TraPPE-UA. The temperature in this set of simulations ranges from 25 to 55°C;
2. OPLS-AA predicts more accurately the density of cycloalkanes compared to TraPPE-UA. However, the deviation from experimental values is higher for this group compared to linear and branched alkanes. The temperature in this set of simulations ranges from 10 to 55°C;

3. TraPPE-UA predicts more accurately the density of benzene and naphthalene. This force field predicts density values within 0.5% of the experimental values. Whereas, the latter has deviations in the order of 4% for benzene and 7% for naphthalene. The temperature in this set of simulations ranges from 25 to 427°C;
4. In the case of oxane, where the temperature ranges from 20 to 50°C, and OPLS-AA predicts better the density compared to TraPPE-UA;
5. For the rest of the hetero-molecules, the deviation from experimental values is high especially for OPLS-AA. It reaches 17% for thiophene, 22% for pyrrole and 15% for pyridine where the temperature ranges from 100 to 300°C.

4.1.2. Structural Analysis

In the asphalt molecules shown in Figures 2-5, fused rings form the bulk of the structures, whereas, linear and branched chains are attached to the edges. Due to the hindrance effects, the fused rings will remain planar and only the linear chains will be free to move. Therefore, the radial distribution function and the dihedral angle distribution of n-pentane, which can accurately represent the peripherals, will be studied at ambient conditions. The respective plots are shown in Figures 13 and 14. The atomic diameter for both force fields is around 0.36 nm, below which the g(r) is zero. This is due to the strong repulsive forces between atoms. The first peak occurs at 0.6 nm, with the g(r) being equal to 1.4, i.e. on average, each molecule is surrounded by 1.4 molecules at this distance. The g(r) approaches a value of 1 at a distance of 1.05 nm and beyond. This indicates that beyond this distance, the fluid exhibits mean field behavior.

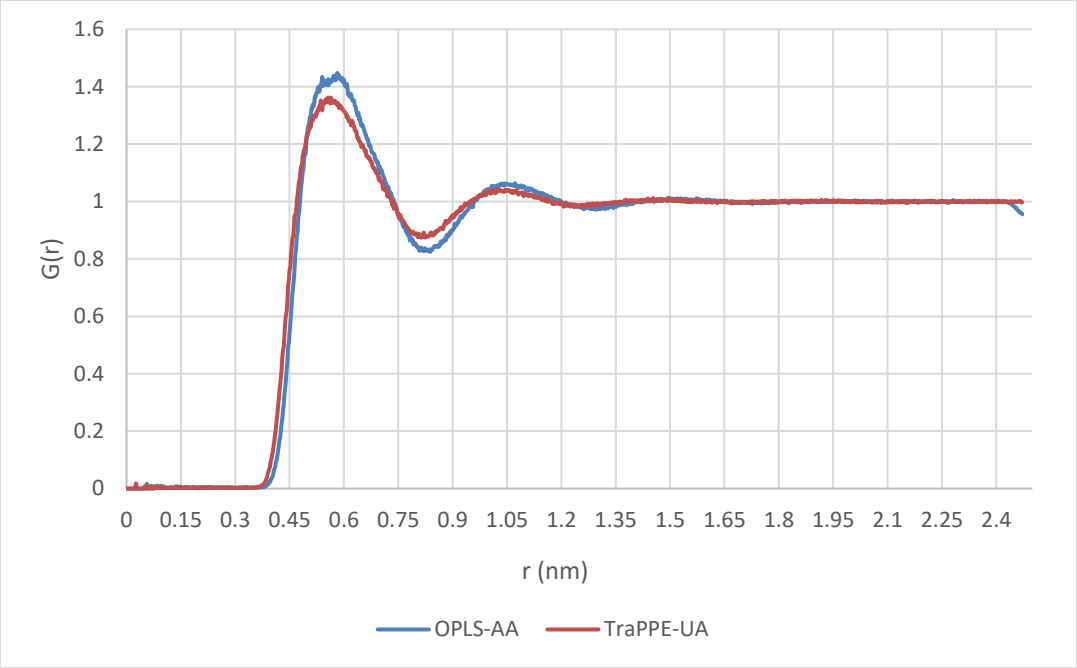

Figure 13: Radial distribution function of n-pentane at ambient conditions

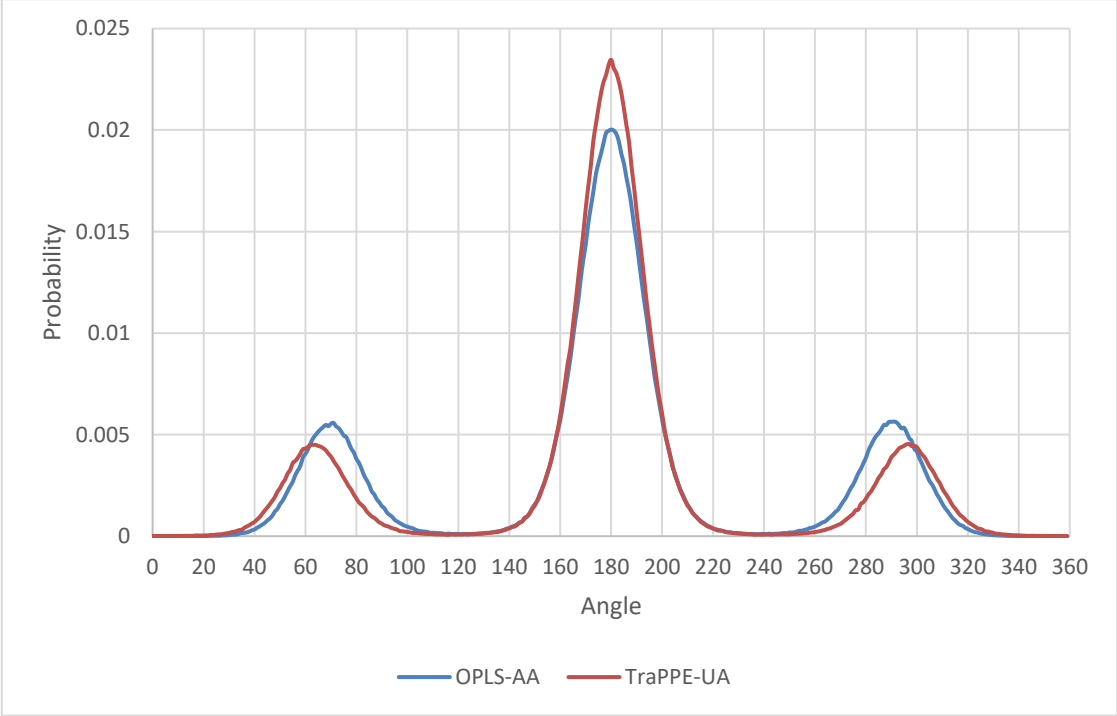

Figure 14: Dihedral angle distribution of n-pentane at ambient conditions

The C-C-C-C dihedral angle distributions of n-pentane using both OPLS-AA and TraPPE-UA show a large peak at 180° corresponding to the trans conformation and two smaller peaks at around 70° and 290°, 60° and 300° respectively corresponding to the gauche conformations (with local energy minima). The trans population is closer to the experimental value (70.7%)[54] for TraPPE-UA (71.3%) compared to OPLS-AA (64.6%).

Overall, TraPPE-UA predicts more accurately the density of the 12 different components because the force field is parametrized for each group of molecules differently. Whereas, OPLS-AA is a general force field that is parametrized for a general set of molecules and ions. The error in the density obtained by OPLS-AA show a general trend: It increases when the temperature is higher than 100°C and when we go from alkanes to benzene and naphthalene to 5-ring hetero-molecules such as pyridine, thiophene and pyrrole. In addition, TraPPE-UA predicts more accurately the structural properties of alkanes than OPLS-AA does. Despite the results obtained, it is impossible to build the complex structures of the asphalt model using TraPPE-UA because the fused rings should be kept planar and their parameters must be optimized. Therefore, we will rely on OPLS-AA to simulate our asphalt model in the rest of this thesis. In addition, the temperature will be kept within 150°C because we already proved that the force field works better at lower temperatures.

4.2. Asphalt Molecular Structure

To create AS1, the arithmetic $\overline{MW}$ was used. The mole fractions for the various components within each class were equal. However, a more complex approach was used to construct the AS2 model. More emphasis was given to components of high molecular

weight, i.e. higher mole fractions were assigned to higher molecular weight molecules. Table 2 summarizes the exact composition of the developed asphalt models, AS1 and AS2.

Table 2: Composition of the AS1 and AS2 models

Class	Acronym	$MW_{i,j}$ (kg/kmol)	x_j		$\overline{MW_i}$ (kg/kmol)		$N_{i,j}$	
			AS1	AS2	AS1	AS2	AS1	AS2
Saturates	HOP	482.9	0.5	0.92	452.9	478.1	40	69
	SQU	422.8	0.5	0.08			40	6
Aromatics	DOC	406.7	0.5	0.07	435.7	460.7	76	10
	PHP	464.7	0.5	0.93			76	133
Resins	QLH	553.9	0.2	0.125	467.2	506.9	7	4
	TIR	573.0	0.2	0.500			7	16
	BBT	290.4	0.2	0.125			7	4
	PYH	503.9	0.2	0.125			7	4
	TBO	414.7	0.2	0.125			7	4
Asphaltenes	MOA	574.9	0.33	0.1875	723.5	795.6	6	3
	MOB	888.4	0.33	0.6250			6	10
	MOC	707.1	0.33	0.1875			6	3

The SARA weight fractions of the two model asphalts, AS1 and AS2 compare well to the experimental values as shown in Table 3. The weight fractions of both models are within 1% from the experimental values. In addition, the elemental composition of asphaltic models is another important aspect. Carbon is the most abundant element in asphalt binders (79-88 wt. %), followed by hydrogen (7-13 wt. %).[55] Traces of heteroatoms (up to 8 wt. %) are also found in binders.[55] The elemental composition of both asphalt models is shown in Table 4.

Table 3: SARA weight fraction comparison

Class	$SARA_{exp}$ wt. %	$SARA_{AS1}$ wt. %	AS1 % absolute error	$SARA_{AS2}$ wt. %	AS2 % absolute error
Saturates	27.43	27.48	0.19	27.44	0.03
Aromatics	50.36	50.24	0.24	50.41	0.10
Resins	12.42	12.40	0.14	12.41	0.07
Asphaltenes	9.80	9.88	0.80	9.74	0.60

Table 4: Asphalt models' elemental composition

Asphalt Model	Weight Percent					H/C ratio
	C	H	O	N	S	
AS1	87.78	11.19	0.16	0.21	0.66	1.52
AS2	88.43	10.63	0.09	0.19	0.66	1.43

The carbon content, being around 88%, is at the higher experimental limit; whereas, the heteroatoms content of approximately 1% is at the lower limit. The SARA analysis and elemental composition of both models, AS1 and AS2, are similar. Therefore, we need another property such as density to differentiate between the models.

4.3. Equilibration Analysis

Eight different initial configurations were randomly generated for each model. The AS1 and AS2 initial structures were cubic cells of 285 and 266 molecules and a density of 0.219 and 0.217 g/cm^3 respectively. After applying the equilibration protocol, one needs to inspect if the system is well equilibrated in terms of density, potential energy and pressure and well relaxed in terms of structural properties such as the autocorrelation function for the end-to-end distance of the different molecules. Figures 15 and 16 show

the final equilibrated structures of one of the configurations for models AS1 and AS2 respectively at 25°C for illustrative purposes. The different colors represent different molecules.

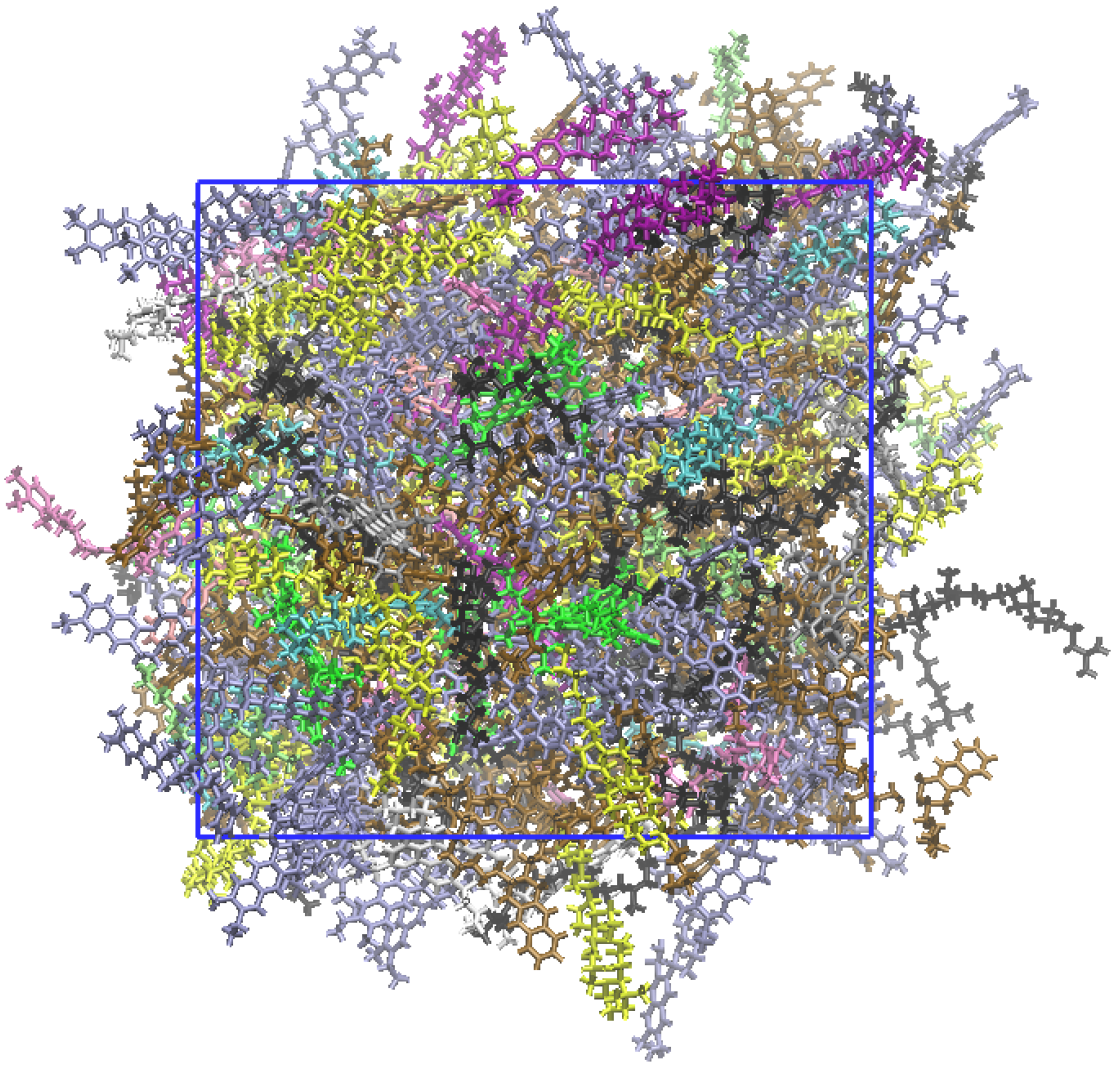

Figure 15: AS1 equilibrated structure at 25°C

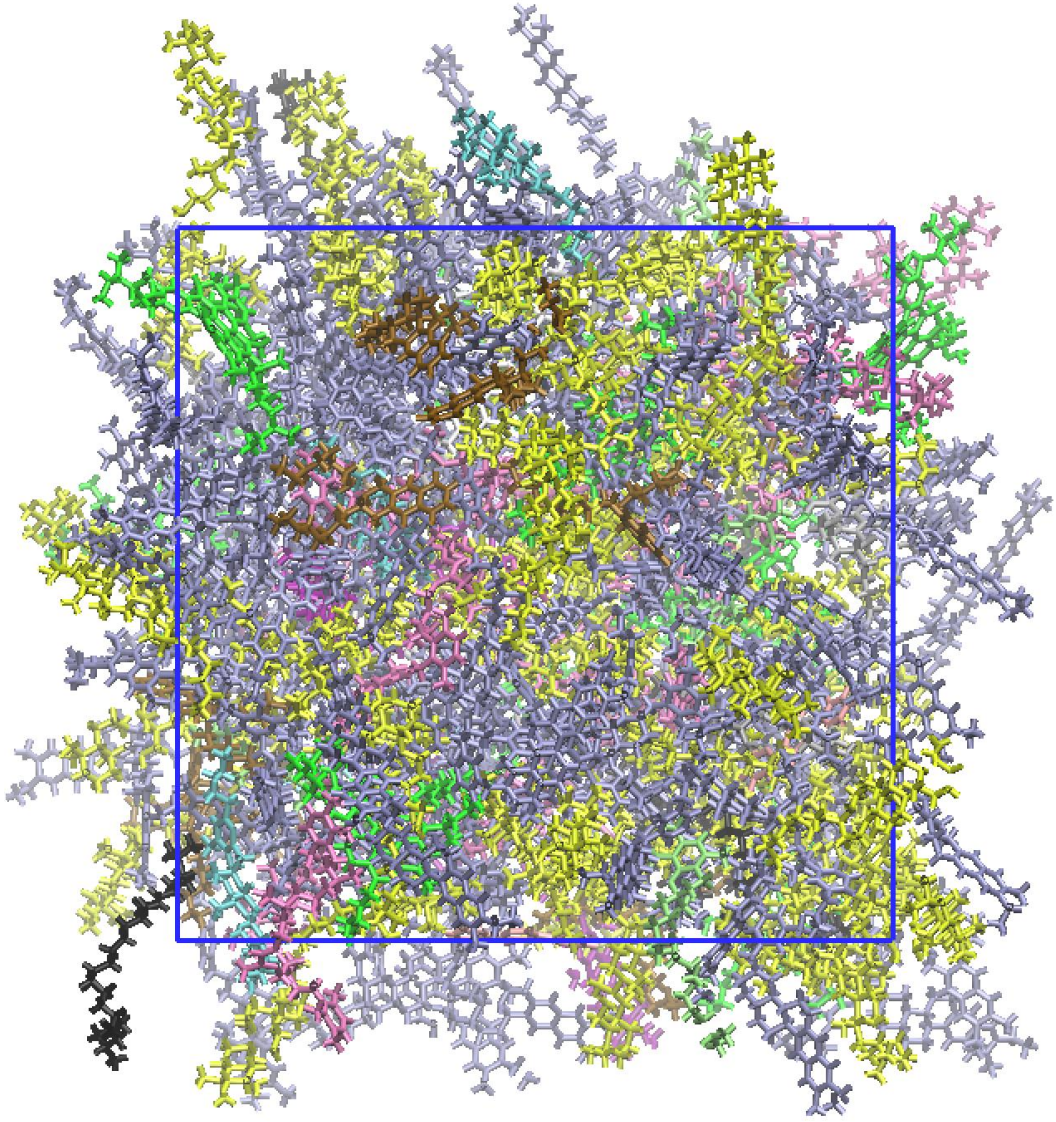

Figure 16: AS2 equilibrated structure at 25°C

4.3.1. Density

The average density at 25°C was calculated and compared to the experimental value of 1005 kg/m^3.[42] It was found that the density of AS1 is 963 (± 2) kg/m^3 and that of AS2 is 988 (±1) kg/m^3. The relative error percent is higher for AS1 than AS2 (4.2% > 1.7%). Therefore, we will choose the AS2 asphalt model to be used in this research. The

evolution of the density with time was recorded for the eight different configurations at 25, 50, 75, 100, 125 and 150°C. The running averages at 25, 50 and 75°C were plotted. The three temperatures are of interest because the mechanical properties will be later studied at these same temperatures.

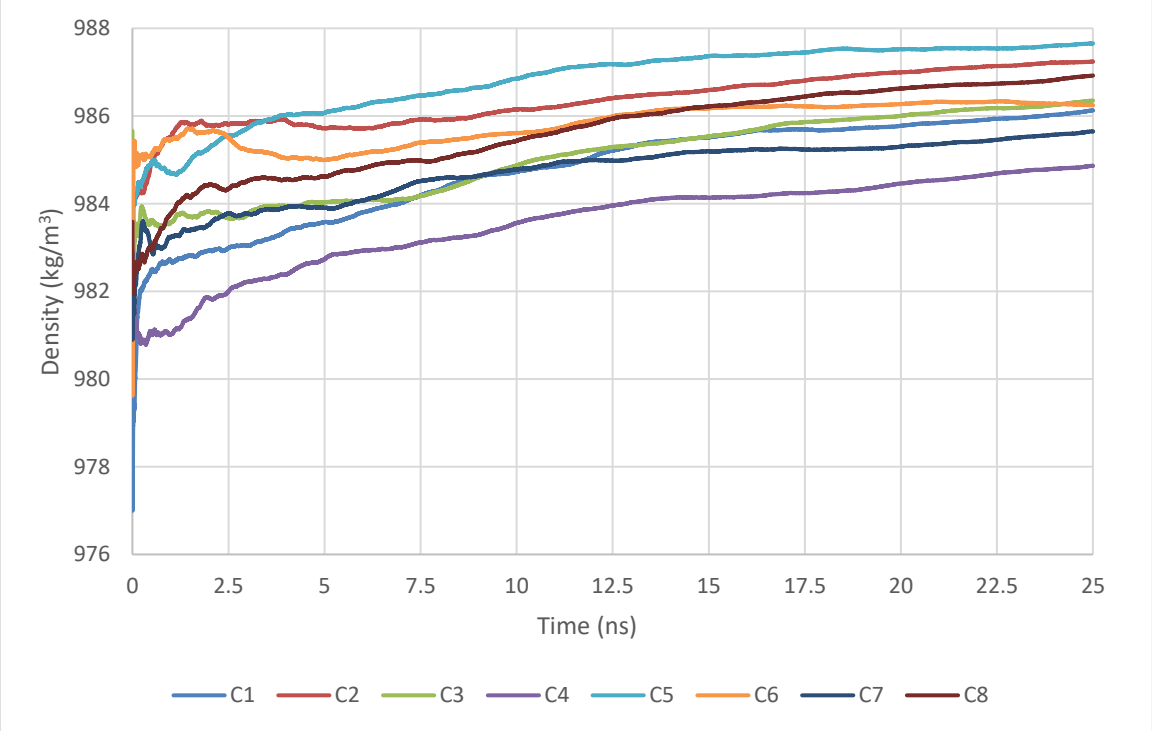

Figure 17: Density equilibration profile at 25°C

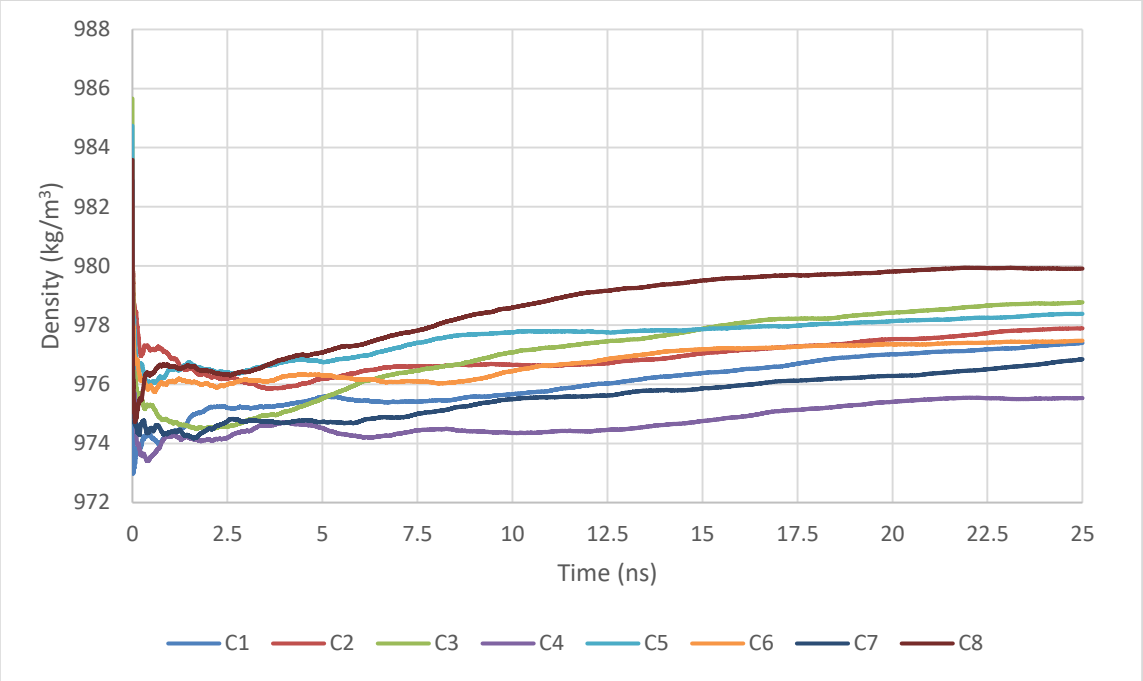

Figure 18: Density equilibration profile at 50°C

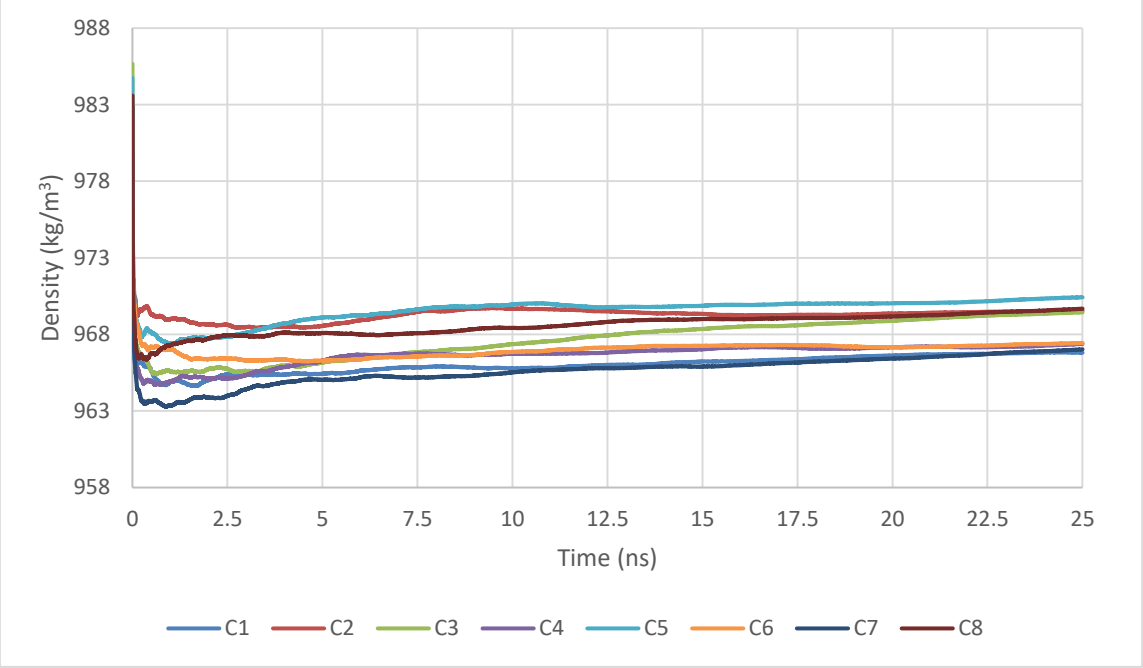

Figure 19: Density equilibration profile at 75°C

By inspecting the running averages in Figure 17-Figure 19, one can see that at 25°C, the eight different configurations have not reached equilibrium yet after 25 ns. Hence, the density was not yet equilibrated. On the other hand, at 50 and 75°C, the density equilibration profiles show a smooth plateau after a 22.5 ns and 20 ns respectively.

4.3.2. Potential Energy

Many terms contribute to the potential energy of the system: Lennard-Jones potential, Coulombic interactions, bonds, angles and dihedrals.[41] A constant potential energy with time indicates that the sum of the aforementioned inter- and intramolecular interactions is fluctuating around an average value, hence the system has reached equilibrium. The evolution of the potential energy with time was recorded for the eight different configurations at 25, 50, 75, 100, 125 and 150°C. The running averages at 25, 50 and 75°C for the last 2 ns were plotted against time in Figures 20-22.

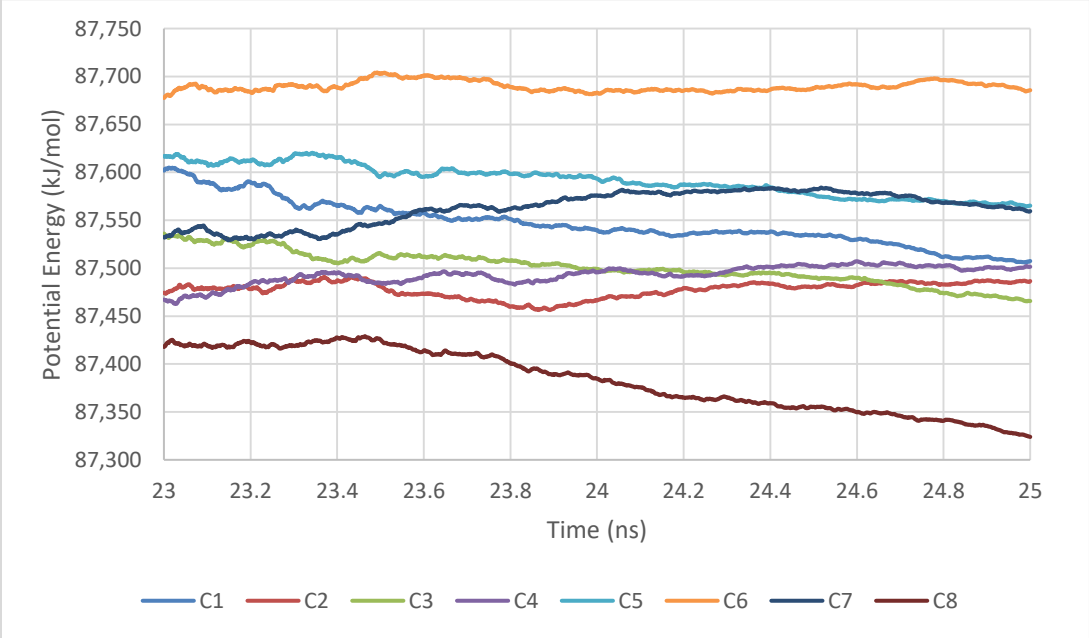

Figure 20: Potential energy equilibration profile at 25°C

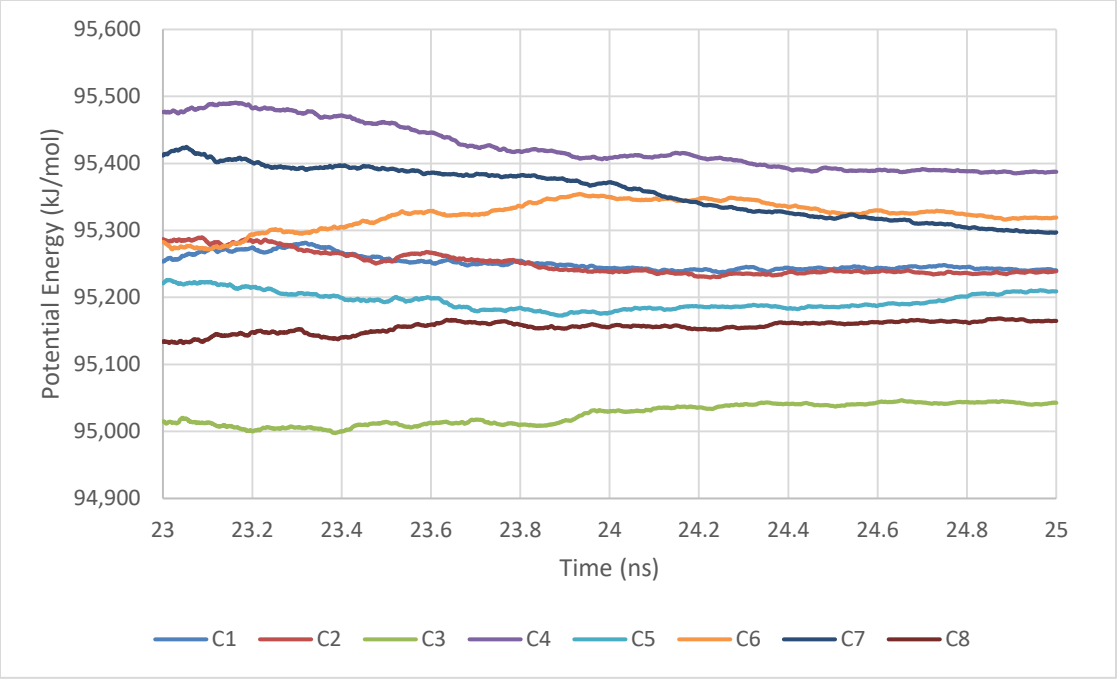

Figure 21: Potential energy equilibration profile at 50°C

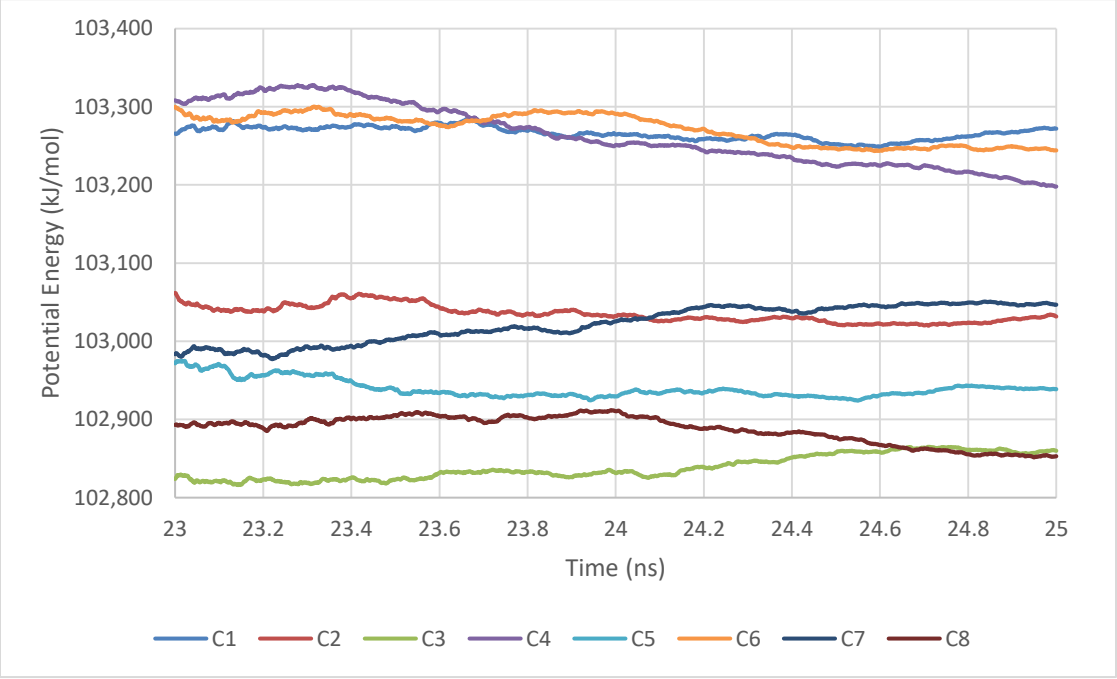

Figure 22: Potential energy equilibration profile at 75°C

These potential energy graphs are in good agreement with the density profiles. It is obvious that the potential energy at 25°C is still decreasing. At 50 and 75°C, the potential energy has reached equilibrium, and this is shown by the plateaus formed after a 25 ns run.

4.3.3. Pressure

Our aim was to equilibrate the system at ambient pressure, 1.013 bar. However, the obtained pressures could reach up to 30 bars as shown in Figures 23-25. The pressure values are expected to be high especially when using the Berendsen barostat. This barostat is only used for equilibration purposes not for obtaining exact values.[41] This is shown by the results obtained. The pressure of the system at all temperatures and for all configurations is equilibrated.

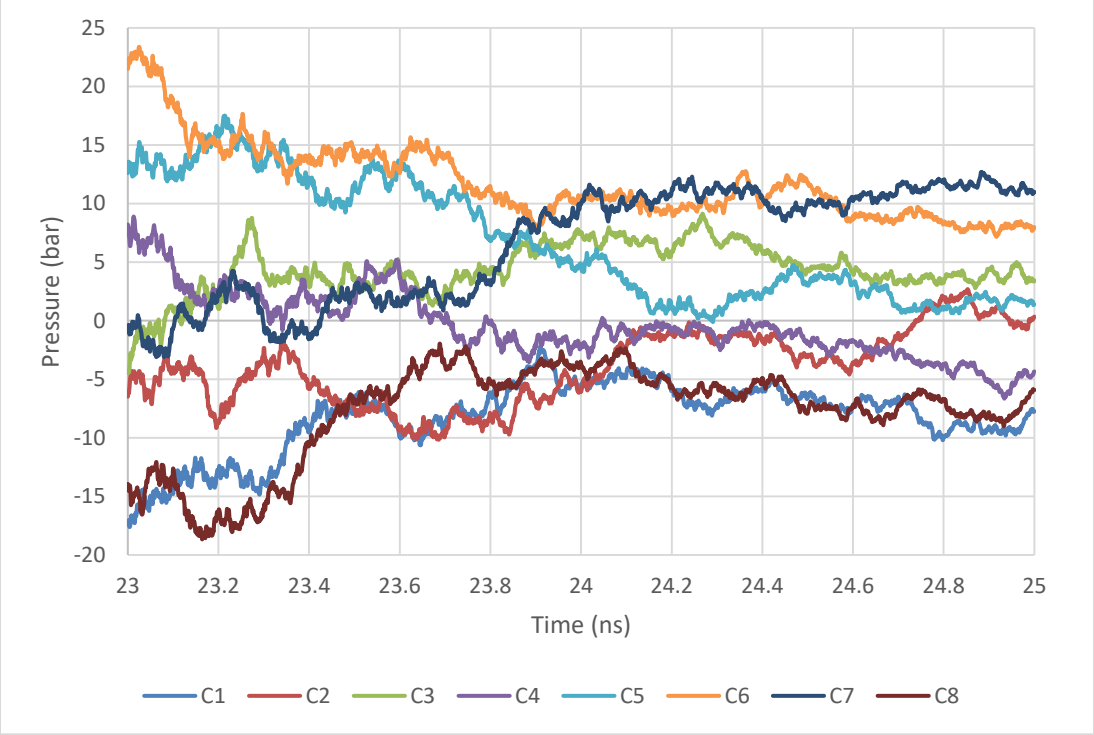

Figure 23: Pressure equilibration profile at 25°C

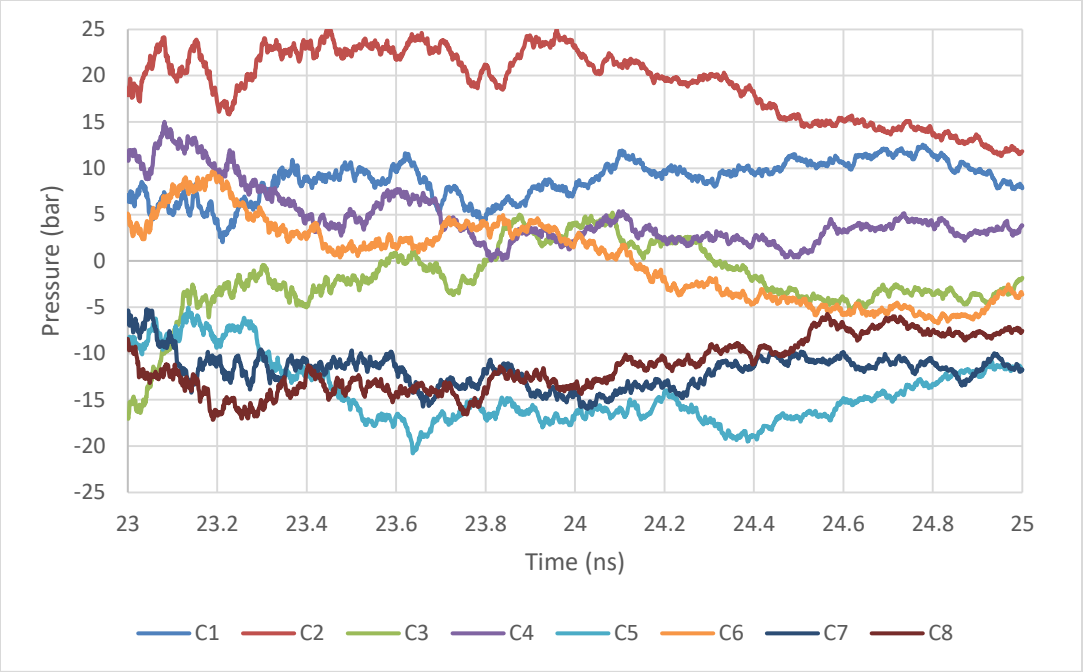

Figure 24: Pressure equilibration profile at 50°C

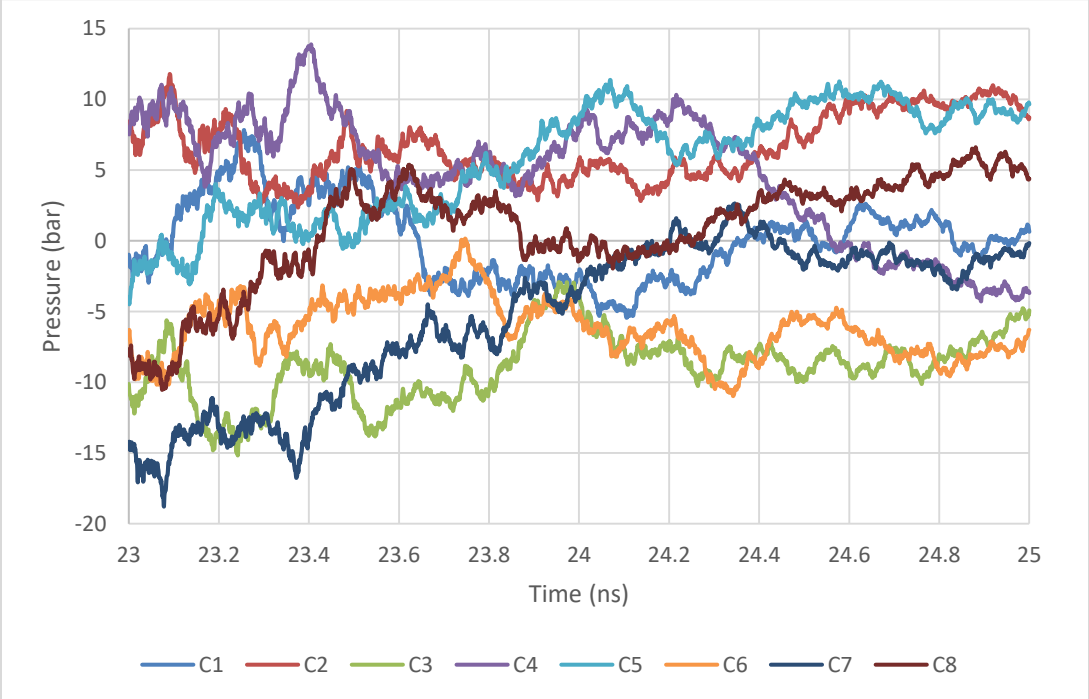

Figure 25: Pressure equilibration profile at 75°C

In an attempt to equilibrate the systems at 25°C and reduce the pressures, two extra steps were introduced to the general equilibration protocol. The system underwent another annealing round followed by a 15 ns NPT simulation. In the latter, the six components of the pressure tensor were decoupled.

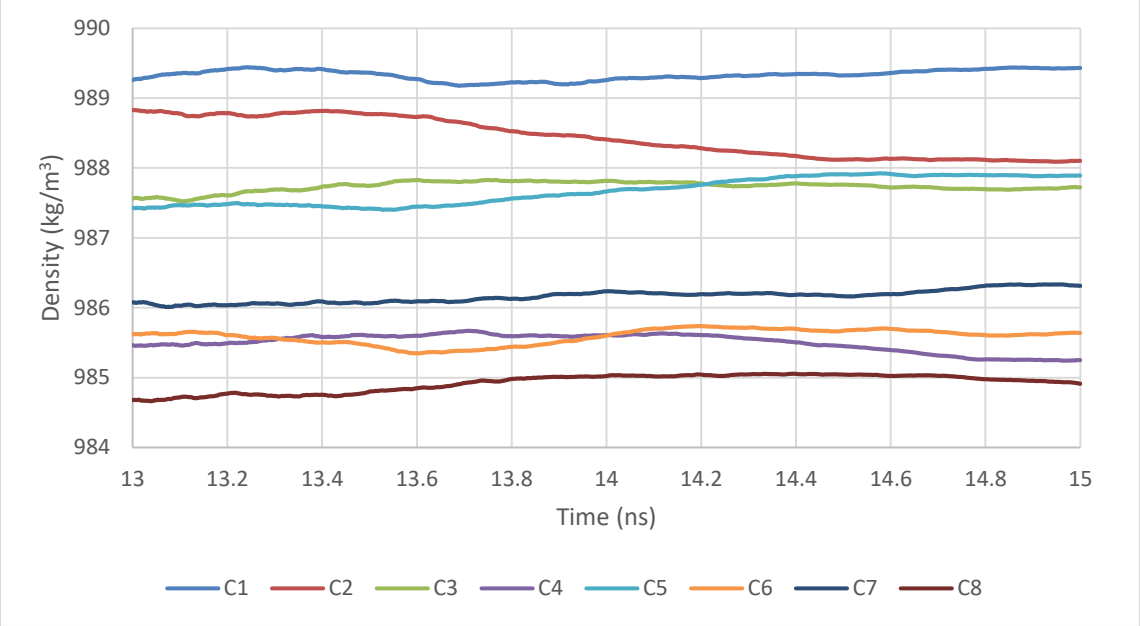

Figure 26: Density extended equilibration profile at 25°C

The extended equilibration density profile shows that the density is finally equilibrated for all configurations. The average value was found to be 987 (± 2) kg/m^3, which is the same as before adding the other two steps. The potential energy profile in Figure 27 agrees with the density profiles. The structures are well equilibrated in terms of PE. However, the pressure showed the same trend as before, the numbers are almost the same and the pressure is still considered high. Yet, the pressure is well equilibrated.

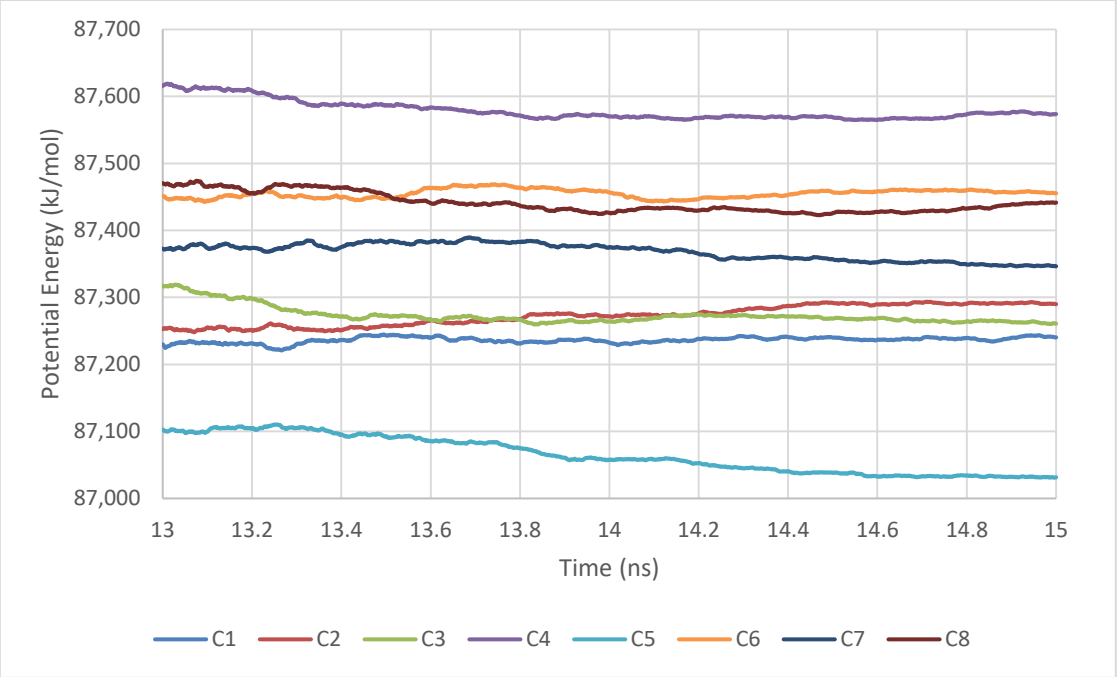

Figure 27: Potential energy extended equilibration profile at 25°C

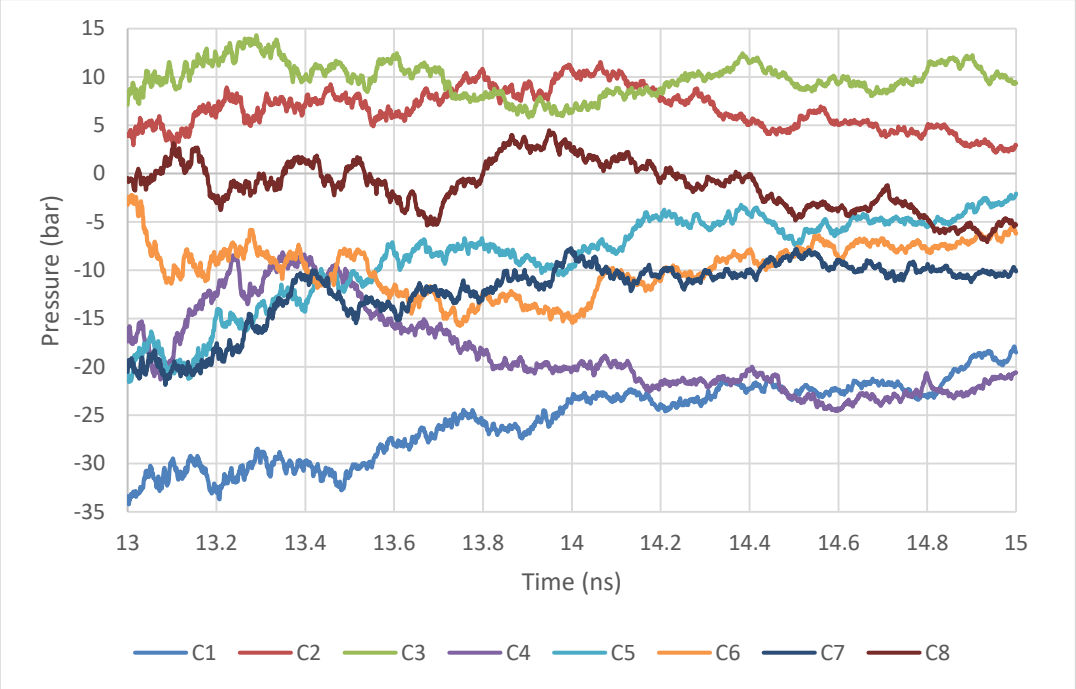

Figure 28: Pressure extended equilibration profile at 25°C

After the system has been equilibrated at 25°C, the average density was calculated at each temperature to obtain the density variation with respect to temperature.

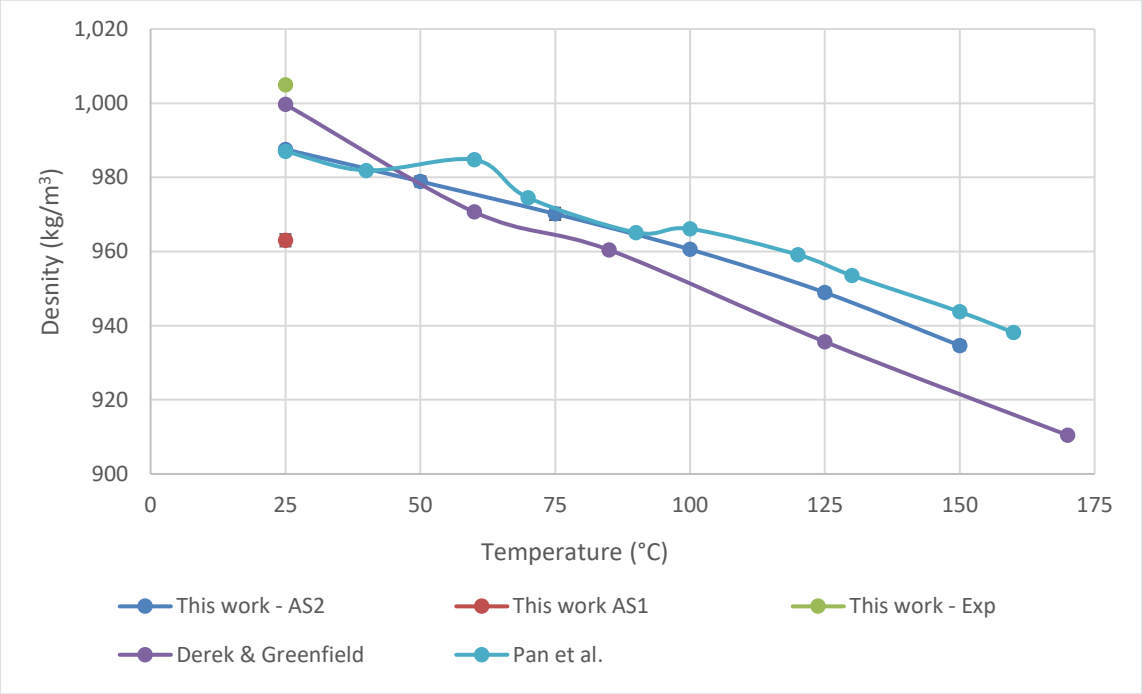

Figure 29: Density profile with respect to temperature

Figure 29 presents the density as function of temperature for this work, as well as Derek and Greenfield[9] and Pan et al[56]. It is evident from the results that the density decreases with increasing temperature for all simulation models. The AS2 model is in good agreement with the other two simulation models. However, the AS2 curve is smooth and continuous compared to the other two curves, which is an improvement over these models. It allows the interpolation of the density at temperatures lower than 25°C and higher than 150°C. It turned out that after decoupling the six components of the pressure tensor, the equilibrated structures were triclinic cells not orthorhombic anymore.

However, this shift was minimal. If one ought to visualize the structures, one cannot see the difference.

4.3.4. Autocorrelation Function

The autocorrelation function for the end-to-end distance indicates whether a structure is relaxed or not. The developed asphalt model is comprised of linear molecules such as squalane, bulky molecules such as asphaltenes and other molecules that share both characteristics. Figure 30 shows the autocorrelation function of squalane and asphaltene-B for the 1st and 2nd steps of the equilibration process.

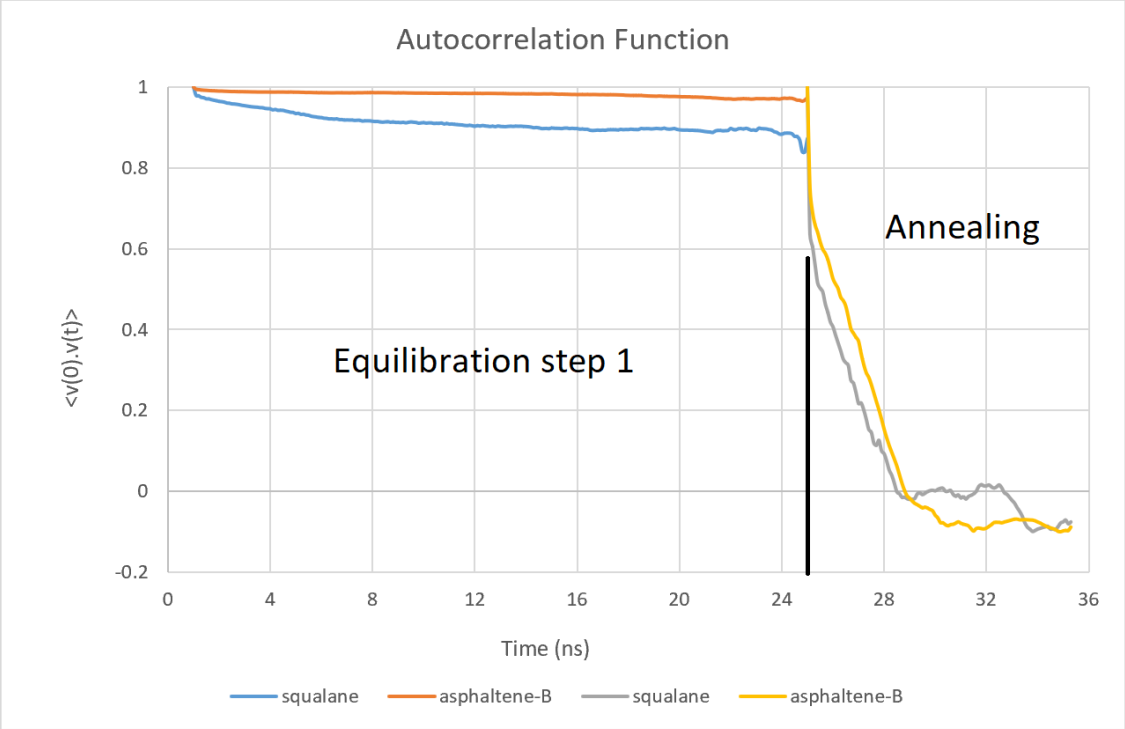

Figure 30: Autocorrelation function of squalane and asphaltene-B

The 1st equilibration step was carried out at 25°C, a temperature at which the molecules don't move and are not relaxed as shown above. Therefore, implementing an annealing

procedure right after, would totally relax the structures. The autocorrelation function goes to zero for both types of molecules.

4.3.5. Cohesive Energy Density

We were able to obtain the cohesive energy density as a function of temperature. The negative values indicate that attraction forces are greater than the repulsive forces. It can be inferred from Figure 31 that the absolute value of cohesive energy density of the system decreases with increasing temperature. This indicates that at higher temperatures, the attraction forces are becoming weaker. This could be because the simulation box becomes bigger in volume at higher temperatures and the molecules are further apart.

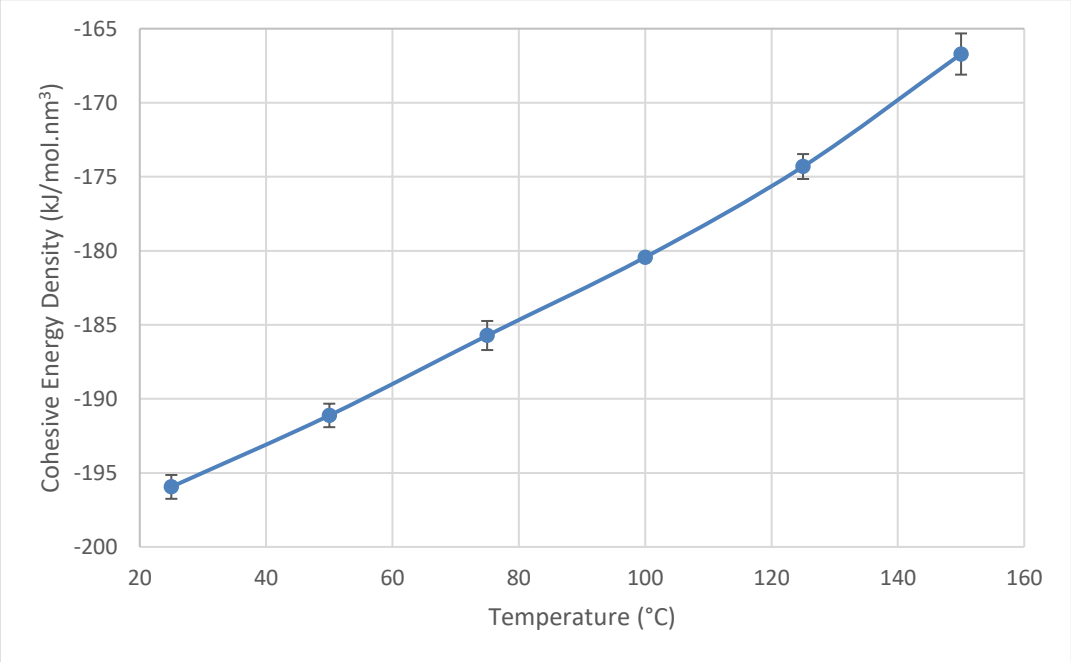

Figure 31: Cohesive energy density profile with respect to temperature

4.4. Mechanical Properties

At 25℃, the Theodorou and Suter and the stress-strain methods were applied on both types of structures, orthorhombic and triclinic in an attempt to compare the results based on the structures and the methods. The hydrostatic compression and uniaxial tension fits from the Theodorou and Suter method for both structures are shown in Figures 32-39.

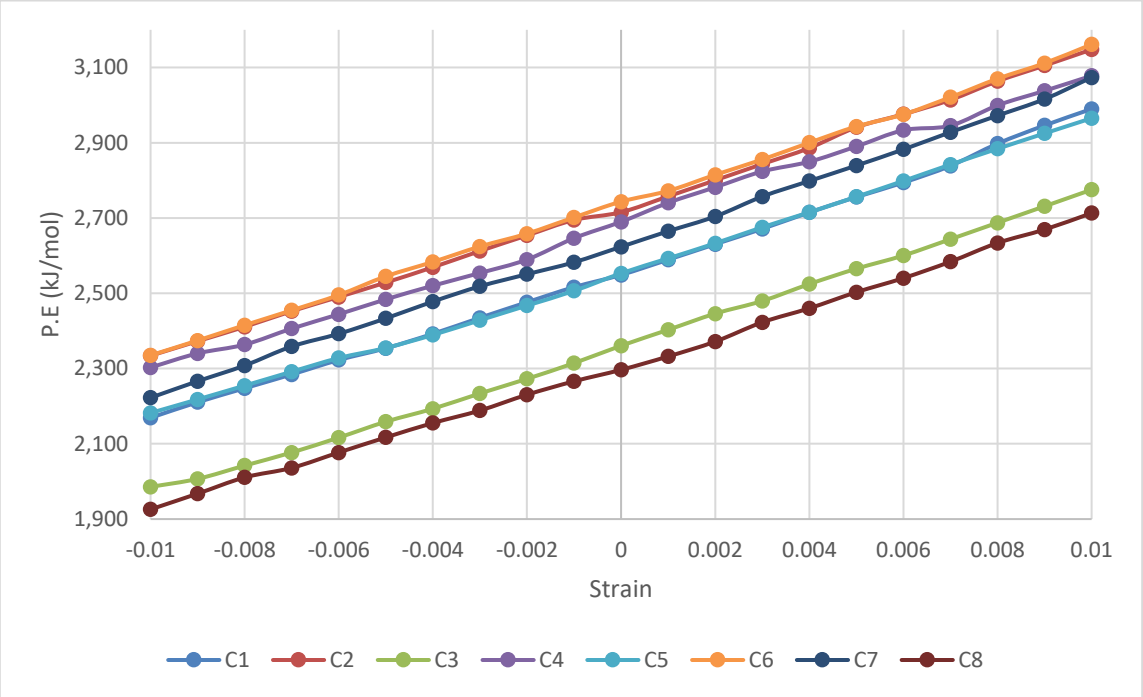

Figure 32: Hydrostatic compression of the orthorhombic structure

The orthorhombic and triclinic hydrostatic compressions fail to yield smooth second-degree polynomial fits. Theoretically, the potential energy (P.E.) should increase with increasing strain. However, in Figure 32, only configurations 1, 3, and 5 show such a trend. In the rest of the configurations, the potential energy fluctuates. These fluctuations could be major such as in C4, where the P.E. increases within the strain range of -0.002 and 0.003 then decreases again at different rates; or minor such as in C8, where P.E.

increases within the strain range of -0.01 and -0.008, then decreases for only one value and then increases again. Overall, in the orthorhombic structure, the majority of the configurations show minor fluctuations with the exception of C2 and C4. In Figure 33, the potential energy of all configurations fluctuates. In the triclinic structure, the majority of the configurations show major fluctuations with the exception of C3 and C8.

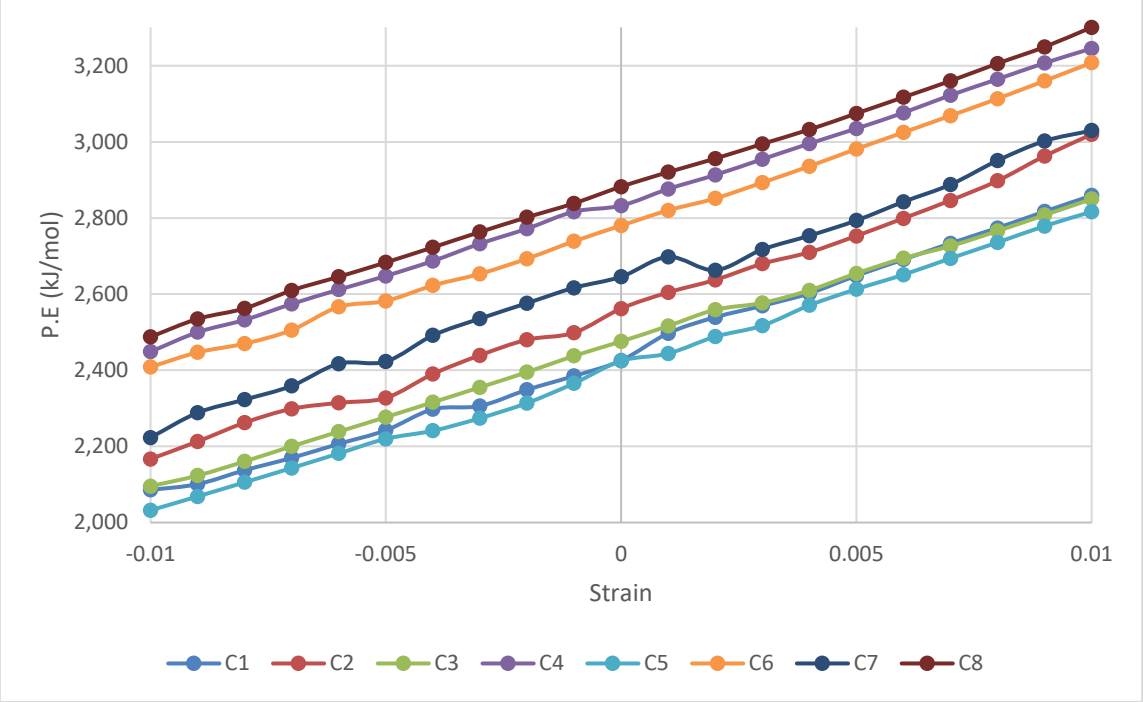

Figure 33: Hydrostatic compression for the triclinic structure

The same trends can be shown for the uniaxial tensions in the x, y and z-directions for the orthorhombic and triclinic structure. Figures 34-36 confirm that C2 and C4 fluctuates the most in the orthorhombic structure. Figures 37-39 also prove that for the triclinic structure, the majority of the configurations fluctuate a lot with the exception of C3 and C8. The poor fits with the quadratic functions verify that for the majority of the

systems, and especially in the triclinic case, the potential energy could not be minimized in response to the deformation within the number of steps assigned.

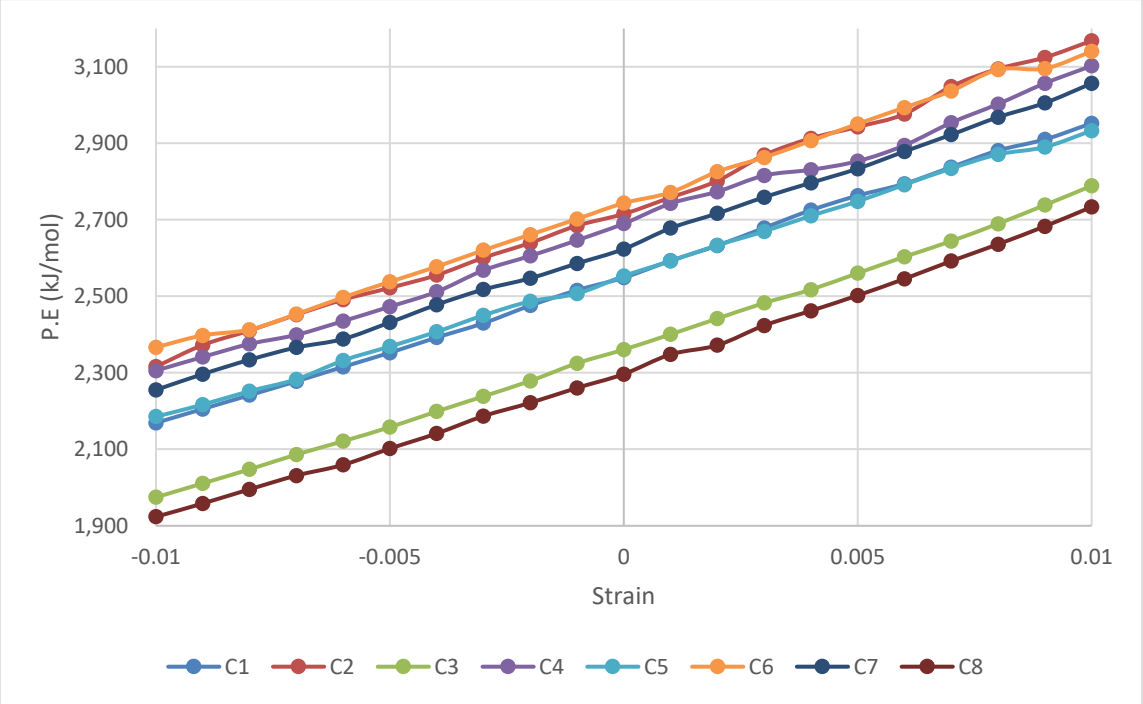

Figure 34: Uniaxial tension in the x-direction of the orthorhombic structure

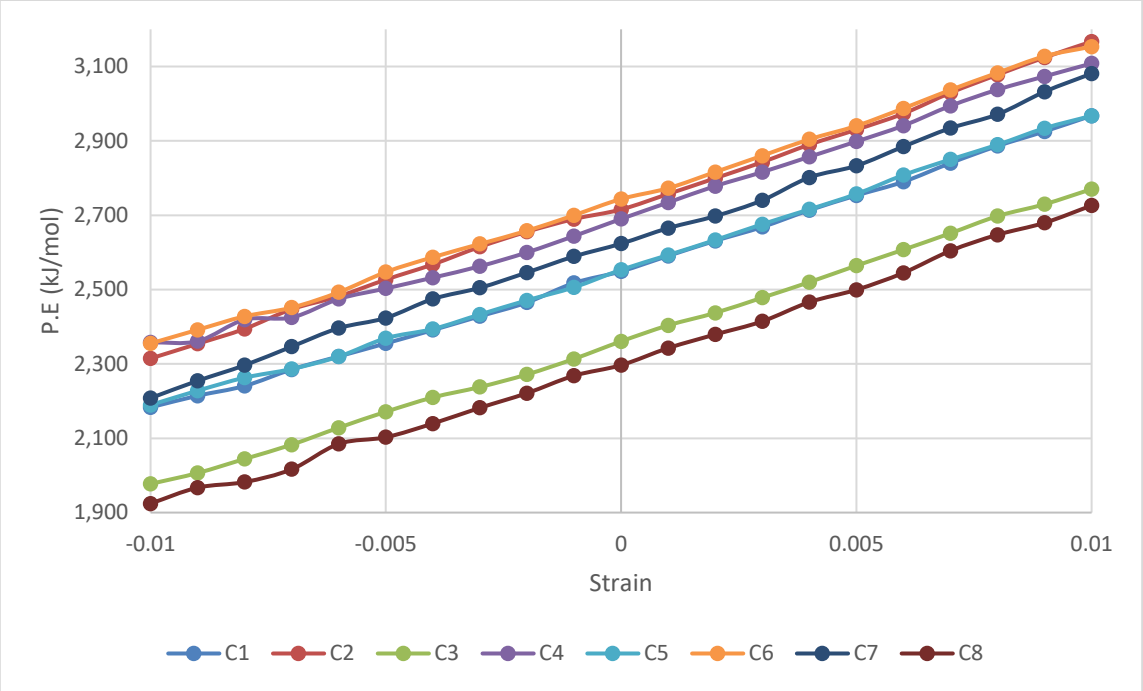

Figure 35: Uniaxial tension in the y-direction of the orthorhombic structure

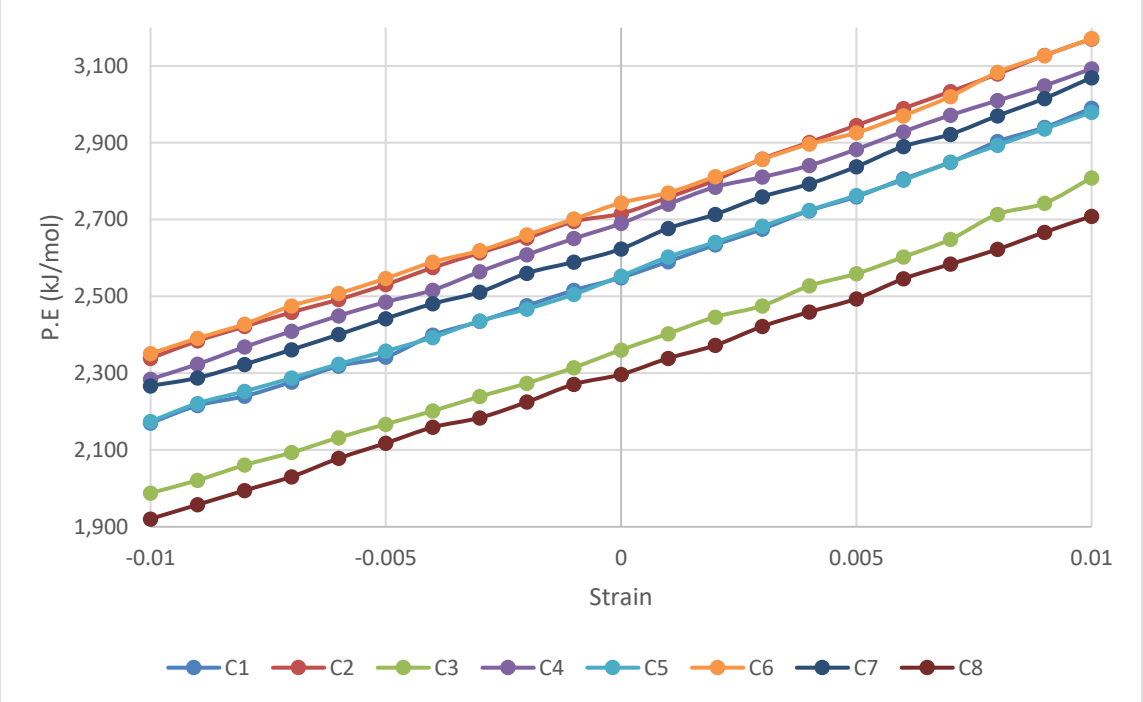

Figure 36: Uniaxial tension in the z-direction of the orthorhombic structure

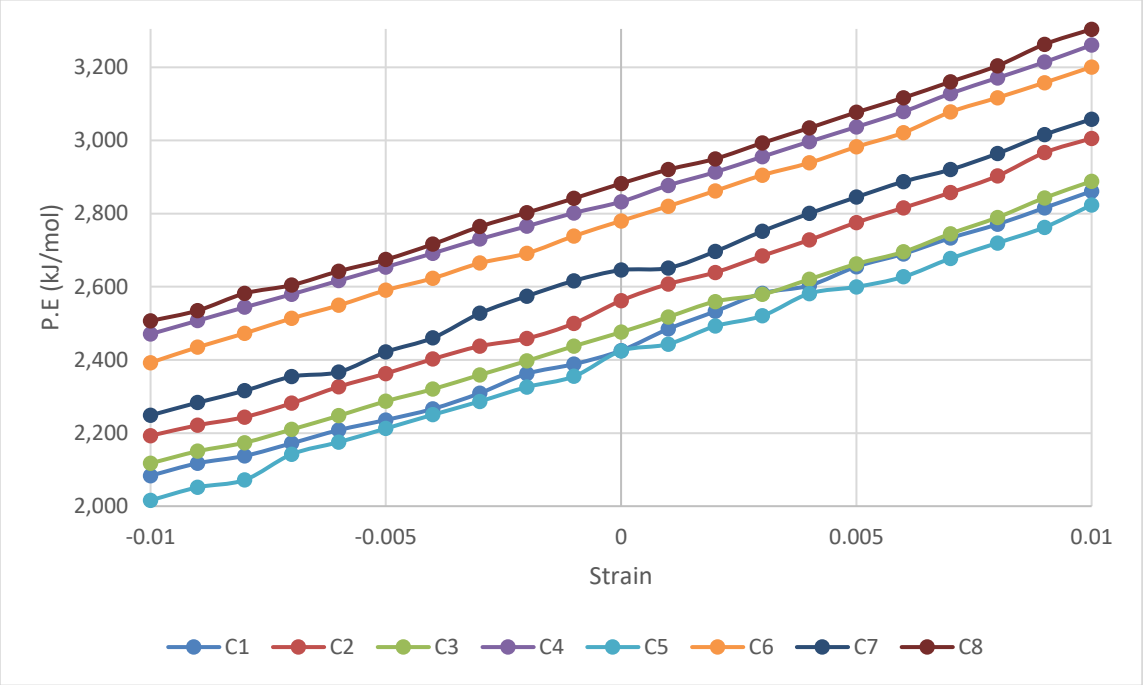

Figure 37: Uniaxial tension in the x-direction of the triclinic structure

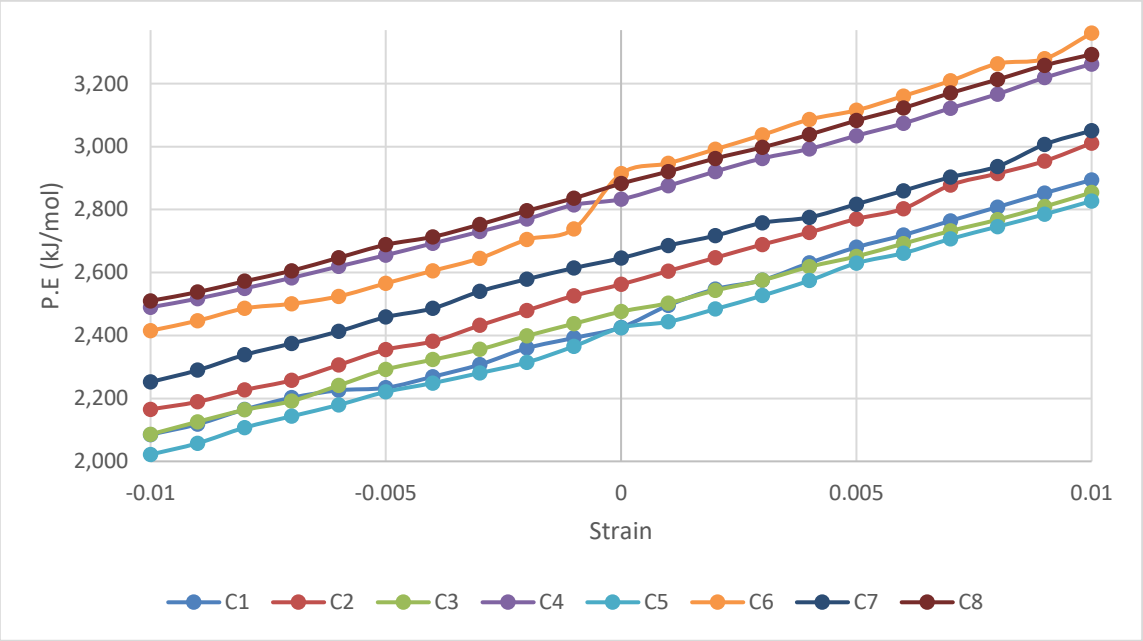

Figure 38: Uniaxial tension in the y-direction of the triclinic structure

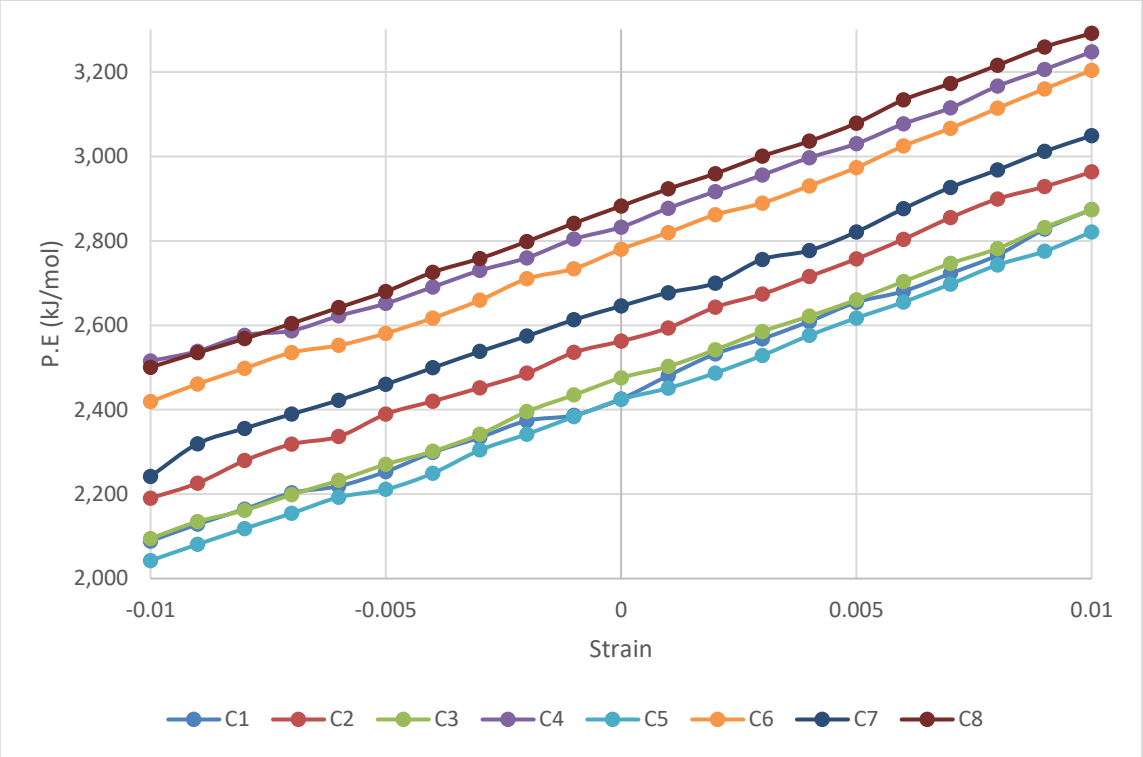

Figure 39: Uniaxial tension in the z-direction of the triclinic structure

The mechanical properties will be derived by plotting the average potential energy with respect to strain over all configurations as shown in Figures 40 and 41.

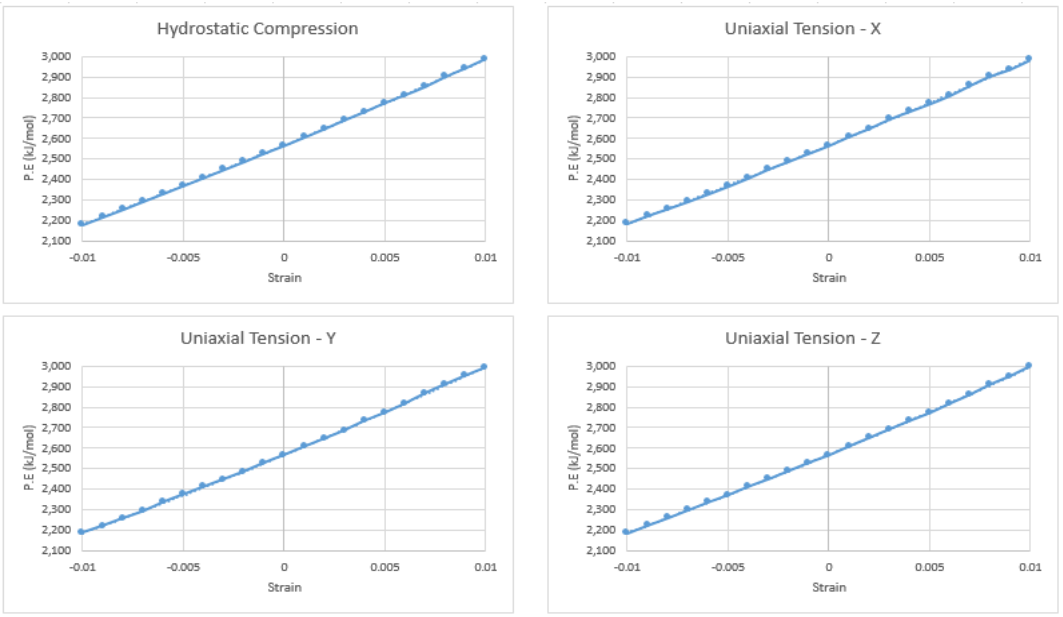

Figure 40: Average plots for the orthorhombic structure

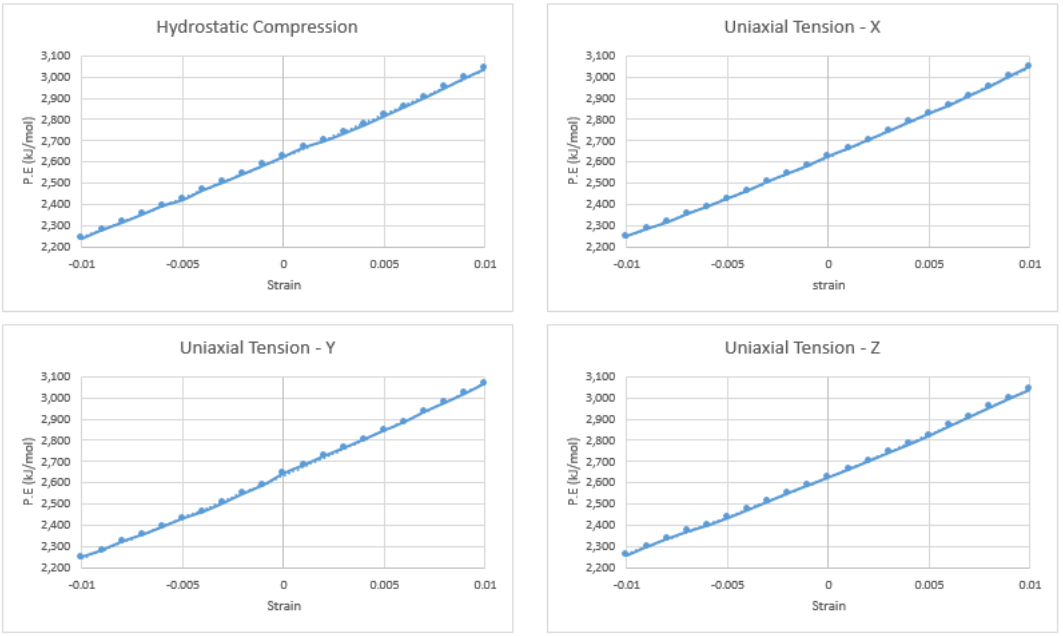

Figure 41: Average plots for the triclinic structure

The mechanical properties deduced from these plots are represented in Table 5.

Table 5: Mechanical properties for the Theodorou and Suter method

Direction	Orthorhombic		Triclinic	
	E (MPa)	ν	E (MPa)	ν
X	-12	0.50	1924	0.39
Y	2544	0.34	1372	0.42
Z	2083	0.37	2626	0.34
Average	1593	0.40	1985	0.38

The elastic modulus show large deviations between the different directions that could be due to the relatively small size of the system or the use of a nonsufficient number of configurations.[48] The molecular distribution of these small systems vary considerably in different directions. Therefore, the response to the stress in different directions is expected to be different. The statistical nature of the systems produced could be overcome by increasing the number of configurations. As a conclusion, the Theodorou and Suter method is highly dependent on the minimization of the potential energy of the system.

The same analysis was implemented using the stress-strain method. Figure 42 is an example on how this method works. A 2.5% continuous strain has been applied on configuration 1 of an orthorhombic structure in the x-direction. The black points represent the instantaneous pressure in the x-direction, which is equivalent to the stress. By applying the adjacent-averaging over 500 points, we obtain the red curve.

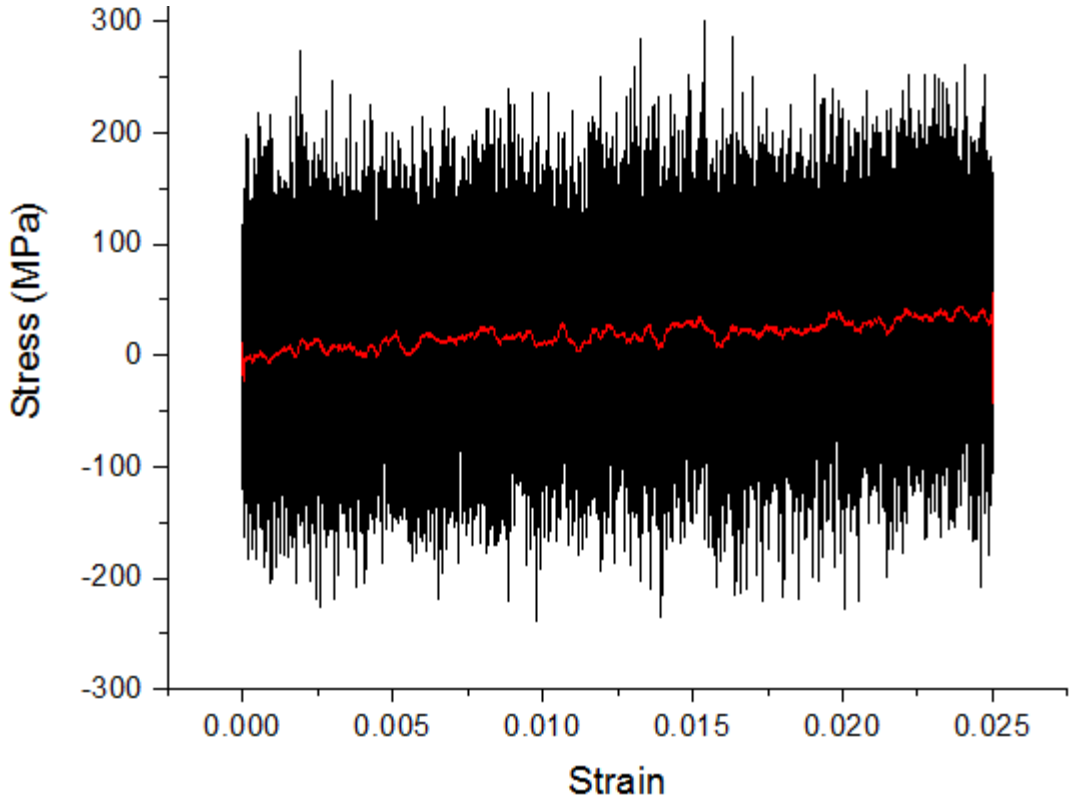

Figure 42: Configuration 1 orthorhombic x-direction stress-strain experiment

This adjacent-averaging was repeated for the seven other configurations to obtain the rest of the smoothened curves. The average over the eight smoothened curves is plotted as shown in Figure 43 and then fitted to a straight line, the slope of which represents the Young's modulus in the x-direction. The same procedure was applied in the other two directions to obtain the average Young's modulus for the orthorhombic structure.

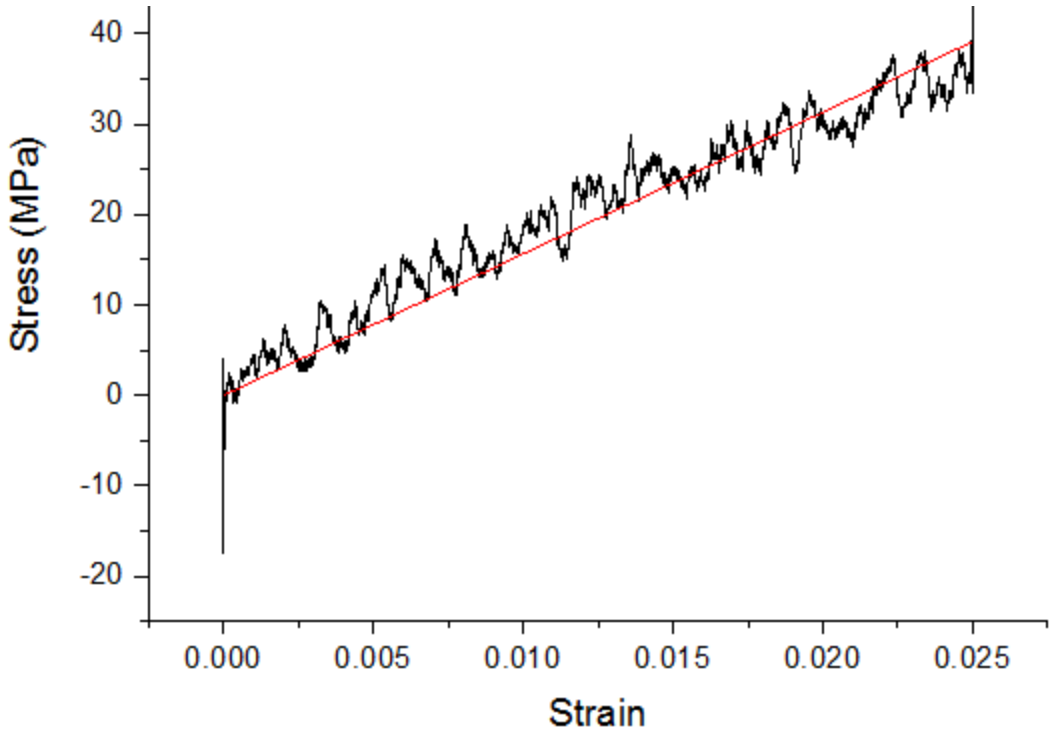

Figure 43: Average stress-strain in the x-direction for an orthorhombic structure

The instantaneous y and z dimensions were plotted against time and smoothened by applying the adjacent-averaging over 50 points as shown in Figures 44 and 45. Then the Poisson ratios in the y and z directions were obtained for configuration 1. The same procedure was repeated for the other configurations to get the average Poisson ratio when the stress is applied in the x-direction. In order to calculate the average Poisson ratios when the stress is applied in the y and z directions, the x and z dimensions and the x and y dimensions were used respectively.

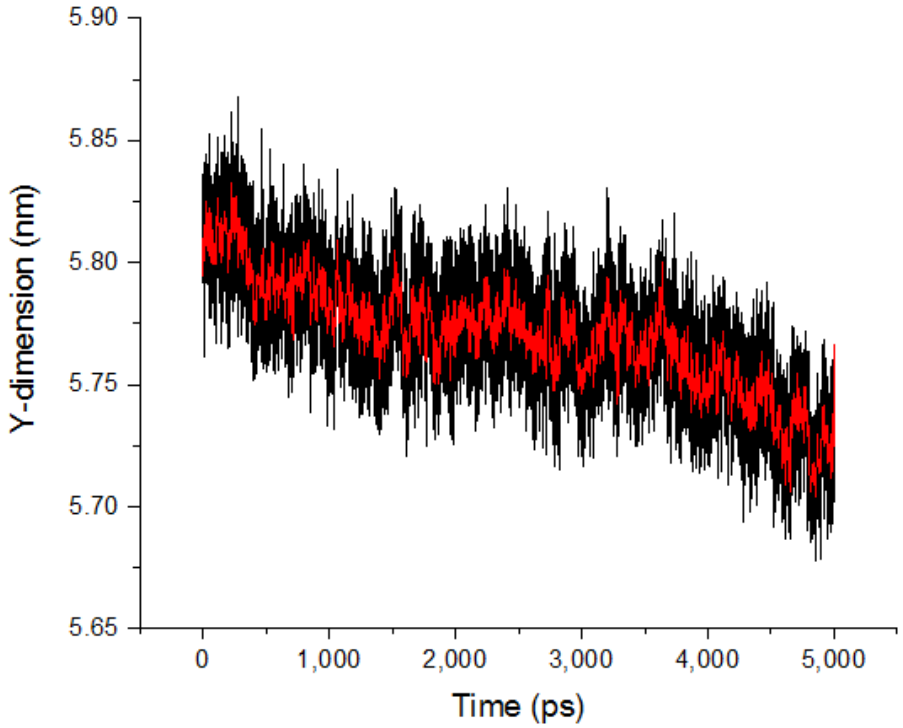

Figure 44: Y-dimension profile with respect to time

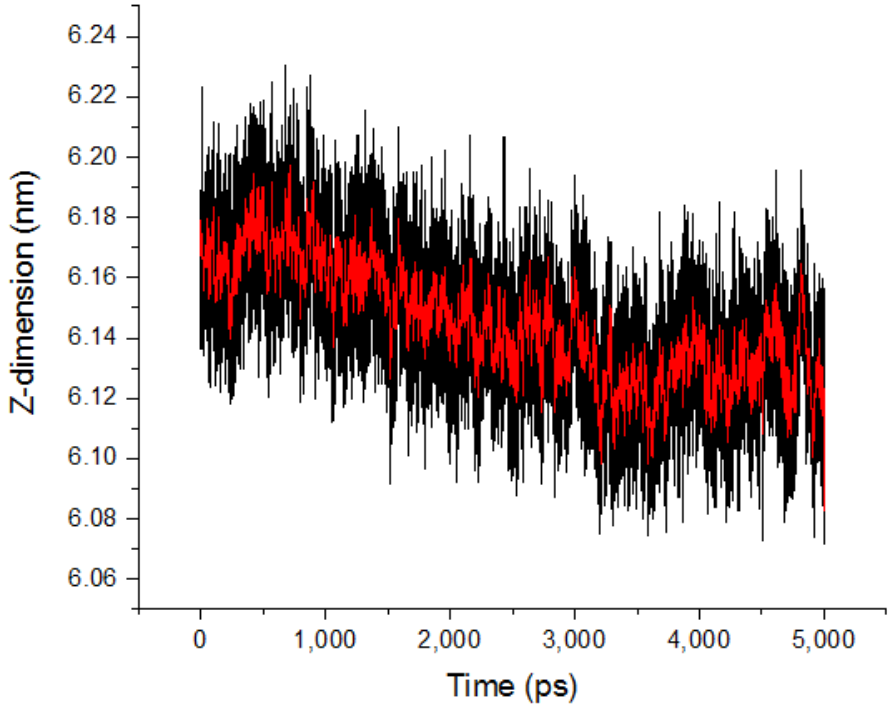

Figure 45: Z-dimension profile with respect to time

The same steps were repeated to obtain the average Young modulus for the triclinic structure. The results are presented in Table 6.

Table 6: Mechanical properties for the stress-strain method

Direction	Orthorhombic		Triclinic	
	E (MPa)	ν	E (MPa)	ν
X	1565	0.40	1416	0.41
Y	1500	0.40	1478	0.40
Z	1449	0.40	1570	0.39
Average	1505	0.40	1488	0.40

Compared to the Theodorou and Suter method, the results of the stress-strain experiment are more accurate. The difference in the Young modulus between the different directions is much lower. Despite the fact that both the orthorhombic and triclinic structures yielded similar results, the mechanical properties at 50 and 75°C will be predicted using the orthorhombic structure. The results are shown in Table 7.

Table 7: Mechanical properties for the stress-strain experiment at 50 and 75°C

Direction	50°C		75°C	
	E (MPa)	ν	E (MPa)	ν
X	1257	0.39	956	0.42
Y	1506	0.43	1079	0.42
Z	1267	0.40	1036	0.40
Average	1343	0.41	1024	0.41

The Young modulus is in good agreement with the experimental value of the WL asphalt binder: 1384 (± 595) MPa that was obtained at the nanoscale by Atomic Force Microscopy (AFM). Discrepancies could be due to the surface morphology of the experimental sample

that cannot be modeled using MD or to the experimental sweeping frequency that is different than the strain frequency used in MD. Researchers also calculated the bulk modulus of model asphalts using MD simulations at ambient conditions and obtained values comparable to this work (1100 MPa[22], 1600 MPa[14] and 730 MPa[17]). The discrepancies in this case could be due to the different asphalt models and force fields used. From the stress-strain method, we were able to plot the Young's modulus profile against temperature as shown in Figure 46. It is evident that the Young modulus decreases with increasing temperature. Despite the fact that we see a change in the slope at 50°C, nothing can be inferred from the plot regarding the phase change because we are only using three data points.

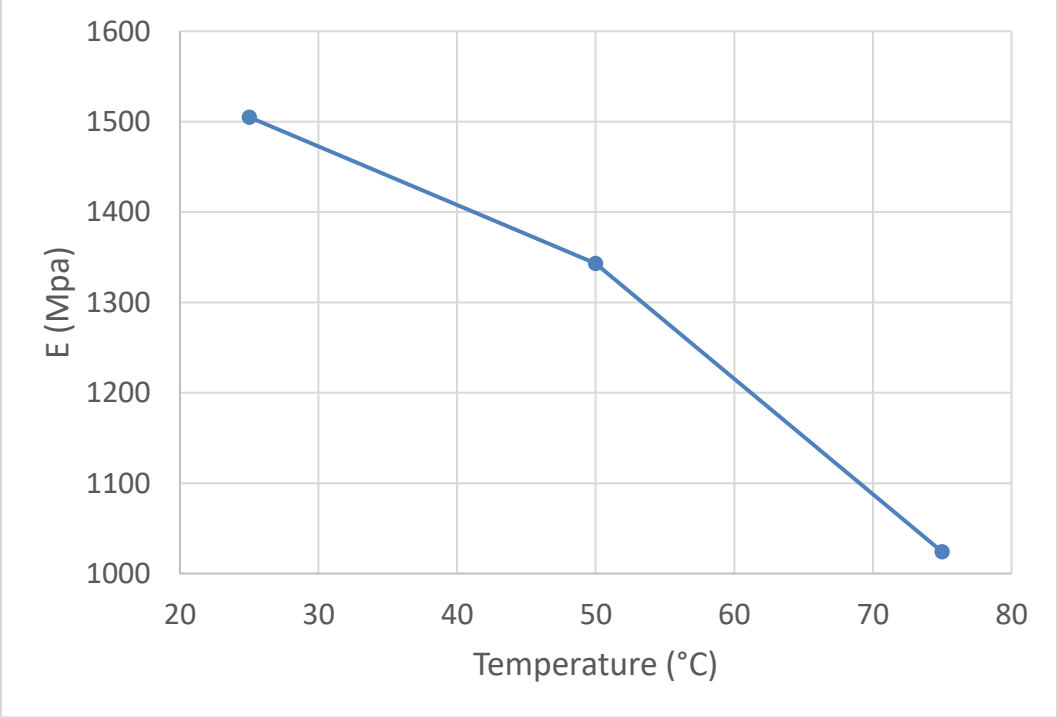

Figure 46: Young's modulus profile with respect to temperature

4.5. Adhesion and Moisture Effects

In the previous sections, the AS2 model was validated against the experimental density and Young's modulus of the WL binder. In this section, the moisture effects on the adhesion between the AS2 asphalt model and two minerals, calcite and quartz, will be evaluated at 25, 50 and 75°C.

4.5.1. Mineral Structures

In order to set up the simulations, there is a need to create realistic calcite and quartz structures.

4.5.1.1. Calcite

In the case of calcite, the $\{10\bar{1}4\}$ structure, shown in Figure 47, was employed for being the most stable and neutral surface.[57] The carbon atom is attached to the oxygen atoms (red) to form a carbonate group. Then the carbonate groups are bound by the calcium atoms (blue). The structure has the following dimensions: $4.99 \times 4.856 \times 2.424\ nm$.

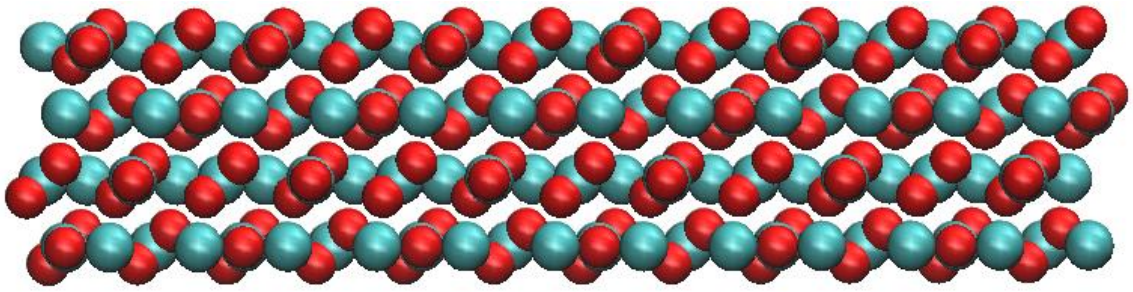

Figure 47: Calcite $\{10\bar{1}4\}$ structure

4.5.1.2. α-Quartz

At ambient conditions of temperature and pressure, α-quartz is the most stable silica polymorph[58] and the $\{001\}$ hydroxylated surface is its most stable surface.[59] The structure shown in Figure 48 has the following dimensions: $4.913 \times 5.106 \times 2.414\ nm$. The tetrahedral silicon (yellow) is attached to the bridging oxygen atoms (red) in the bulk of the structure. At the upper and bottom surfaces, where the structure was cleaved, the hydroxyl oxygen is attached to hydrogen (white).

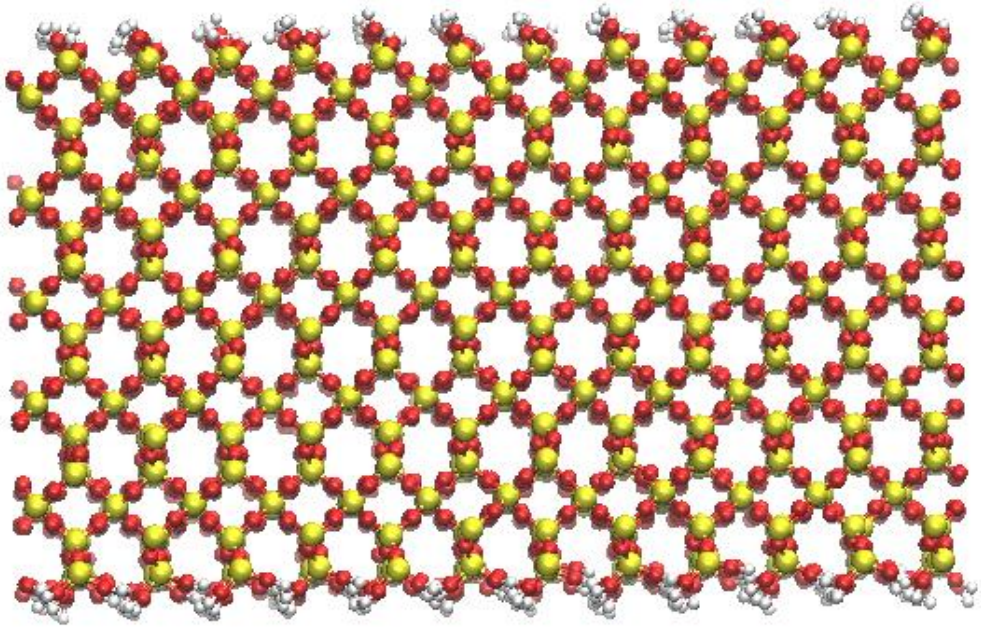

Figure 48: The α-quartz $\{001\}$ structure

4.5.2. Adhesion on a Dry Basis

Asphalt-calcite and asphalt-quartz complex configurations were developed and equilibrated in terms of density and potential energy. Then, the work of adhesion, which is the energy of adhesion per surface area, was calculated by summing up the Coulombic

and Lennard-Jones energies between the asphalt and calcite and quartz respectively then dividing the sum by the surface area at the interface for the three different temperatures. Table 8 summarizes our findings.

Table 8: Work of adhesion at 25, 50 and 75°C on a dry basis

Temperature (°C)	Work of adhesion (kJ/mol.nm^2)	
	Asphalt-Calcite	Asphalt-Quartz
25	-195	-112
50	-197	-104
75	-190	-107

First, the negative values indicate that attractive forces exist between the asphalt structure and both minerals. Second, the work of adhesion was not affected by the temperature increase for either of the minerals. The discrepancies shown in the table are due to the poor statistics; we only used one configuration per temperature. Finally, the obtained results indicate that our asphalt has a higher affinity to bond with calcite than quartz on a dry basis. In their work, Xu and Wang[23] were able to identify the same trend, which was experimentally validated. Minerals of basic nature such as calcite have a stronger adhesion bond with asphalt binders compared to minerals of acidic nature such as quartz[60]. It is worth nothing that around 80% of this adhesion comes from the Lennard-Jones interactions. The rest, which is 20%, is a result of the Coulombic interactions.

4.5.3. Adhesion on a Wet Basis

The asphalt-calcite and asphalt-quartz complex structures were successfully loaded with 438 and 289 water molecules respectively. Figure 49 illustrates the loaded complex structures at 25°C. After equilibrating the complex structures in the presence of water, the number density profile of water in the z-direction for both complex structures were processed at the three different temperatures as shown in Figures 50 and 51.

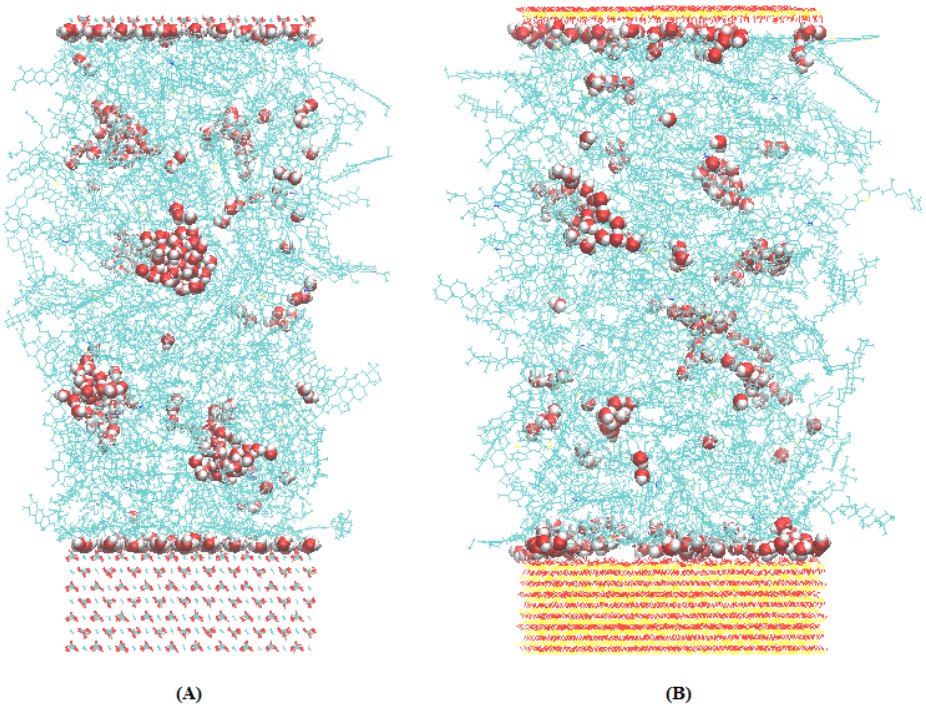

Figure 49: Complex structures with water at 25°C: (A) - calcite, (B) – quartz

The high peaks at the beginning and end of each graph correspond to the number of water molecules at the interface; whereas, the peaks in the middle describe the number of water molecules incorporated in the asphalt structure. In the case of calcite, the number of water molecules at the interface increases significantly with increasing temperature. However,

this is not the case for quartz. The number of water molecules at the interface was approximately the same.

When the temperature is increased, the volume of the asphalt structure increases allowing for more void space. In addition, the kinetic energy of the water molecules increases. Hence, water molecules can diffuse much easier towards the interface, if and only if, the attraction forces between water and the mineral are higher than those of water-water and water-asphalt. The results show that this is true in the case of calcite only. Therefore, water favors the surface of calcite over quartz.

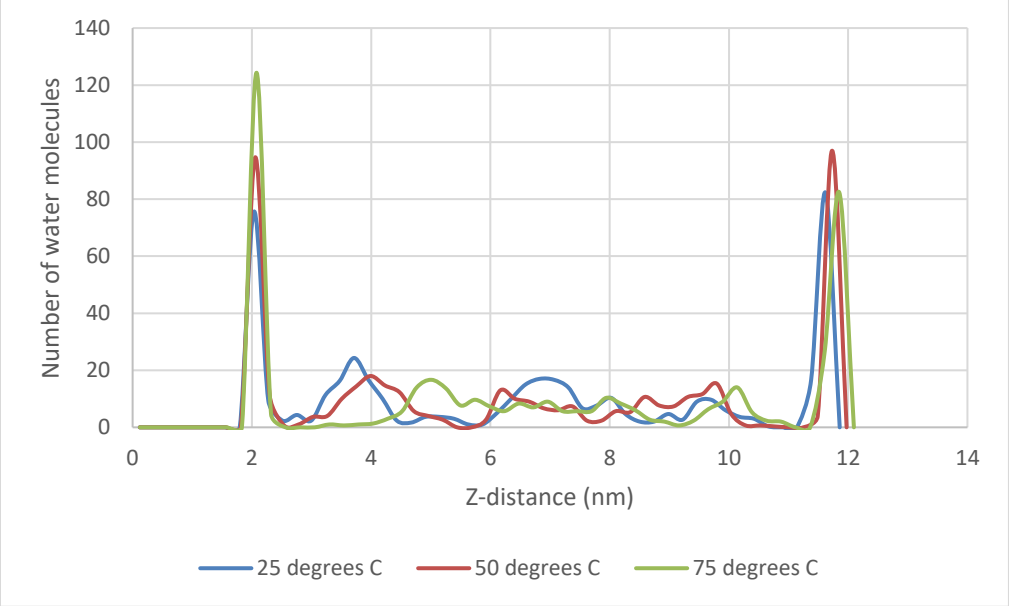

Figure 50: Asphalt-Calcite water number density profile in the z-direction

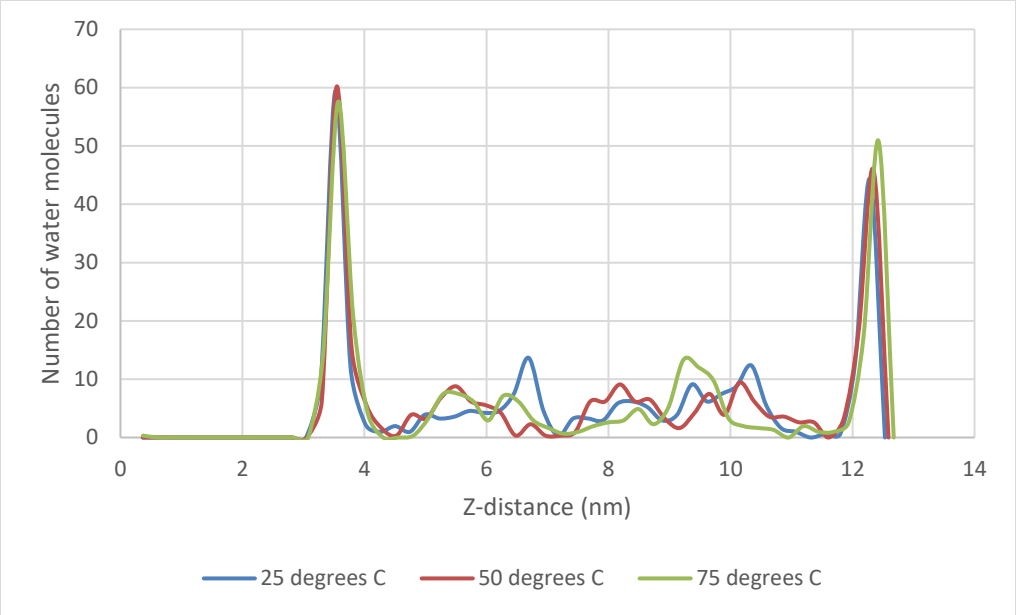

Figure 51: Asphalt-Quartz water number density profile in the z-direction
Table 9 summarizes the results obtained on a wet basis.

Table 9: Work of adhesion at 25, 50 and 75°C on a wet basis

Temperature (°C)	Work of adhesion (kJ/mol.nm^2)	
	Asphalt-Calcite	Asphalt-Quartz
25	-128	-90
50	-115	-85
75	-104	-80

First, we can see that the effect of temperature on calcite is more pronounced compared to quartz. When the temperature increases from 25 to 75°C, the work of adhesion decreases by 19% for calcite and 11% for quartz. This was already established in our previous discussion. In the case of calcite, more water diffuses to the interface at higher temperatures compared to quartz. Second, the work of adhesion on a wet basis has dropped by 41% and 21% for calcite and quartz respectively compared to the work of

adhesion on a dry basis. These results are in good agreement with our findings that water favors the calcite surface over quartz. Finally, even with the higher drop, calcite still has a higher bonding energy to the asphalt binder in the presence of water for all temperatures. Based on these calculations, one can assume that in real life application, the damage will start at the quartz surface. It was already proven experimentally that quartz show a detrimental behavior in presence of moisture[61].

The MD simulations conducted had multiple shortcomings:

- Experimentally, the presence of contaminants and aggregate's surface texture play an important role in the adhesion work. Computationally, these two factors were not accounted for. Therefore, different aggregate surfaces must be used, and contaminants should be added to the complex system;
- The water content for both aggregates was different, which would affect the adhesion forces at the interface. This could be overcome by normalizing the number of water molecules adsorbed at the interface;
- The acid-base reactions taking place at the interface and the hydrogen bonding that might occur between the hydroxyl groups in quartz and water were not accounted for because of the limitations of the Xiao et.al. and CLAYFF force fields. A force field that accounts explicitly for chemical reactions may be more preferable;
- Two different force fields were used for calcite and quartz. The use of one common force field would yield a more accurate comparison. However, such a force field does not exist in the literature.

5. CONCLUSIONS

MD simulations were used to study the effect of moisture on the adhesion forces between a developed model asphalt and mineral structures such as calcite and quartz at the nanoscale. The asphalt model was equilibrated and relaxed by applying a new protocol developed in this study. Simulation data were validated against experimental density and Young's modulus measurements obtained at ambient conditions. The following conclusions emerged from this work:

1. TraPPE-UA predicted the densities of small organic molecules in a range of temperatures and reproduced the structural properties of pentane more accurately than OPLS-AA. However, the general nature of the latter gives it an advantage over TraPPE-UA, that cannot be used to represent asphalt molecules without being further optimized;
2. The developed asphalt model agreed with the experimental SARA fractions (within 1%), elemental compositions (within the range) and density (within 1.7%);
3. Due to the nature of the system and the presence of bulky molecules, a new approach was implemented in order to equilibrate the structures in terms of density, potential energy and pressure and relax the different molecules. It took 3 steps (2 equilibration and annealing) and around 60 ns to accomplish this goal. This procedure can be further optimized to reduce the time needed;
4. The Theodorou and Suter method failed to predict the Young's modulus in both orthorhombic and triclinic structures of the asphalt structure. Whereas, the stress-

strain method predicted the Young's modulus within the experimental range for both types of structures. It is recommended to use the stress-strain method for complex multi-component systems;

5. The work of adhesion, on a dry basis, between the asphalt binder and calcite was higher than that of quartz at 25, 50 and 75°C. Experimentally, asphalts adhere to alkaline surfaces stronger than acidic ones. It was also deduced that the temperature does not affect the work of adhesion on a dry basis. In addition, the Lennard-Jones interactions were accounted for at least 80% of the total work of adhesion;
6. The effect of the temperature on asphalt adhesion with calcite in the presence of moisture was more pronounced than the adhesion with quartz. It was also found that calcite is more susceptible to moisture damage after a decrease of 41% in the work of adhesion after adding water compared to 21% for quartz. However, the asphalt-calcite complex system was still favored over the asphalt-quartz because of the higher absolute value of the work of adhesion. Therefore, for engineering applications, it is predicted that damage will start at the weakest link, which is the quartz.

The method developed in this work can be used in the future to guide the design of improved asphalt - mineral structures with superior mechanical properties in real life applications.

In future work, research should take advantage of the equilibration process. The thermodynamic and elastic properties can be always used to validate

asphalt models. However, when it comes to calculating the work of adhesion, there are important factors that should be taken into consideration such as the morphology of the mineral structures, i.e. the effect of the mineral surface, water diffusion in the asphalt structure and water adsorption at the mineral surface and the force fields used to describe asphalts, minerals and water.

REFERENCES

1. Brown, E.; Kandhal, P.; Roberts, F.; Kim, Y.; Lee, D.; Kennedy, T., Asphalt refining, uses, and properties. In *Hot mix asphalt materials, mixture design and construction*, Third ed.; NAPA Research and Education Foundation: United States of America, 2009; p 720.

2. Brown, E.; Kandhal, P.; Roberts, F.; Kim, Y.; Lee, D.; Kennedy, T., Hot mix asphalt mix design methodology. In *Hot mix asphalt materials, mixture design and construction*, Third ed.; NAPA Research and Education Foundation: United States of America, 2009; p 720.

3. Brown, E.; Kandhal, P.; Roberts, F.; Kim, Y.; Lee, D.; Kennedy, T., Characterization of asphalt mixtures. In *Hot mix asphalt materials, mixture design and construction*, Third ed.; NAPA Research and Education Foundation: United States of America, 2009; p 720.

4. Bhasin, A.; Little, D.; Vasconcelos, K.; Masad, E., Surface free energy to identify moisture sensitivity of materials for asphalt mixes. *Transportation Research Board* **2007**, 37 - 45.

5. Frenkel, D.; Smit, B., *Understanding molecular simulation: from algorithms to applications*. second ed.; Academic Press: 2002; Vol. 1, p 638.

6. Jorgensen, W.; Maxwell, D.; Tirado-Rives, J., Development and testing of the OPLS All-Atom force field on conformational energetics and properties of organic liquids. *Journal of the American Chemical Society* **1996,** *118*, 11225-11236.

7. Jorgensen, W.; McDonald, N., Development of an all-atom force field for heterocycles. properties of liquid pyridine and diazenes. *Journal of Molecular Structure (THEOCHEM)* **1998,** *424*, 145-155.

8. McDonald, N.; Jorgensen, W., Development of an All-Atom force field for heterocycles. properties of liquid pyrrole, furan, diazoles, and oxazoles. *Journal of Physical Chemistry B* **1998,** *102*, 8049-8059.

9. Li, D.; Greenfield, M., Chemical compositions of improved model asphalt systems for molecular simulations. *Fuel* **2014,** *115*, 347 - 356.

10. Corbett, L. W., Densimetric method for characterizing asphalt. *Analytical Chemistry* **1964,** *36* (10), 1967-1972.

11. Corbett, L. W., Composition of asphalt based on generic fractionation, using solvent deasphalting, elution-adsorption chromatography, and densimetric characterization. *Analitical Chemistry* **1969,** *41* (4), 576-580.

12. Brown, E.; Kandhal, P.; Roberts, F.; Kim, Y.; Lee, D.; Kennedy, T., Aggregates. In *Hot mix asphalt materials, mixture design and construction*, Third ed.; NAPA Research and Education Foundation: United States of America, 2009; p 720.

13. Al-Ansary, M.; Iyengar, S. R., Physiochemical characterization of coarse aggregates in Qatar for construction industry. *International Journal of Sustainable Built Environment* **2013,** *2*, 27-40.

14. Zhang, L.; Greenfield, M., Analyzing properties of model asphalts using molecular simulation. *Energy & Fuels* **2007,** *21* (3), 1712-1716.

15. Zhang, L.; Greenfield, M., Molecular orientation in model asphalts using molecular simulation. *Energy & Fuels* **2007,** *21* (2), 1102-1111.

16. Tarefder, R.; Arisa, I., Molecular dynamic simulations for determining change in thermodynamic properties of asphaltene and resin because of aging *Energy Fuels* **2011,** *25*, 2211 - 2222.

17. Pan, J.; Tarefder, R., Investigation of asphalt aging behavior due to oxidation using molecular dynamics simulation. *Molecular Simulation* **2016,** *42*, 667 - 678.

18. Wang, P.; Dong, Z. J.; Tan, Y. Q.; Liu, Z. Y., Investigating the interactions of the saturate, aromatic, resin, and asphaltene four fractions in asphalt binders by molecular simulations. *Energy & Fuels* **2015,** *29* (1), 112-121.

19. Meng, G.; Yiqiu, T.; Linbing, W.; Yue, H., Diffusion of asphaltene, resin, aromatic and saturate components of asphalt on mineral aggregates surface: molecular dynamics simulation. *Road Materials and Pavement Design* **2017,** *18* (sup3), 149-158.

20. Sun, D.; Lin, T.; Zhu, X.; Tian, Y.; Liu, F., Indices for self-healing performance assessments based on molecular dynamics simulation of asphalt binders. *Computational Materials Science* **2016,** *114*, 86-93.

21. Xu, G.; Wang, H., Molecular dynamics study of oxidative aging effect on asphalt binder properties. *Fuel* **2017,** *188*, 1-10.

22. Yao, H.; Dai, Q.; You, Z., Molecular dynamics simulation of physicochemical properties of the asphalt model. *Fuel* **2016,** *164*, 83-93.

23. Xu, G.; Wang, H., Study of cohesion and adhesion properties of asphalt concrete with molecular dynamics simulation. *Computational Materials Science* **2016,** *112*, 161-169.

24. Wang, H.; Lin, E.; Xu, G., Molecular dynamics simulation of asphalt-aggregate interface adhesion strength with moisture effect. *International Journal of Pavement Engineering* **2017,** *18* (5), 414-423.

25. Martin, M.; Siepmann, J., Transferable Potentials for Phase Equilibria. 1. United-Atom description of n-alkanes. *Journal of Physical Chemistry B* **1998,** *102*, 2569-2577.

26. Martin, M.; Siepmann, J., Novel configurational-bias Monte Carlo method for branched molecules. Transferable Potentials for Phase Equilibria. 2. United-Atom description of branched alkanes. *Journal of Physical Chemistry B* **1999,** *103*, 4508-4517.

27. Wick, C.; Martin, M.; Siepmann, J., Transferable Potentials for Phase Equilibria. 4. United-Atom description of linear and branched alkenes and alkylbenzenes. *Journal of Physical Chemistry B* **2000,** *104* (33), 8008-8016.

28. Chen, B.; Potoff, J.; Siepmann, J., Monte Carlo calculations for alcohols and their mixtures with alkanes. Transferable Potentials for Phase Equilibria. 5. United-Atom description of primary, secondary, and tertiary alcohols. *Journal of Physical Chemistry B* **2001,** *105*, 3093-3104.

29. Stubbs, J.; Potoff, J.; Siepmann, J., Transferable Potentials for Phase Equilibria. 6. United-Atom description for ethers, glycols, ketones, and aldehydes. *Journal of Physical Chemistry B* **2004,** *108*, 17596-17605.

30. Wick, C.; Stubbs, J.; Rai, N.; Siepmann, J., Transferable Potentials for Phase Equilibria. 7. primary, secondary, and tertiary amines, nitroalkanes and nitrobenzene, nitriles, amides, pyridine, and pyrimidine. *Journal of Physical Chemistry B* **2005,** *109*, 18974-18982.

31. Lubna, N.; Kamath, G.; Potoff, J.; Rai, N.; Siepmann, J., Transferable Potentials for Phase Equilibria. 8. United-Atom description for thiols, sulfides, disulfides, and thiophene. *Journal of Physical Chemistry B* **2005,** *109* (50), 24100-24107.

32. Dodda, L.; Cabeza de Vaca, I.; Tirado-Rives, J.; Jorgensen, W., LigParGen web server: an automatic OPLS-AA parameter generator for organic ligands. *Nucleic Acids Research* **2017,** *45* (W1), W331-W336.

33. Storer, J.; Giesen, D.; Cramer, C.; Truhlar, D., Class IV charge models: a new semiemperical approach in quantum chemistry. *Journal of Computer-Aided Molecular Design* **1995,** *9*, 87-110.

34. Li, J.; Zhu, T.; Cramer, C.; Truhlar, D., New Class IV Charge Model for extracting accurate partial charges from wave functions. *Journal of Physical Chemistry A* **1998,** *102*, 1820-1831.

35. Thompson, J.; Cramer, C.; Truhlar, D., Parameterization of Charge Model 3 for AM1, PM3,BLYP, and B3LYP. *Journal of Computaional Chemistry* **2003,** *24*, 1291-1304.

36. Kelly, C.; Cramer, C.; Truhlar, D., SM6: a density functional theory continuum solvation model for calculating aqueous solvation free energies of neutrals, ions, and solute-water clusters. *Journal of Chemical Theory and Computation* **2005,** *1*, 1133-1152.

37. Marenich, A.; Olson, R.; Kelly, C.; Cramer, C.; Truhlar, D., Self-consistent reaction field model for aqueous and nonaqueous solutions based on accurate polarized partial charges. *Journal of Chemical Theory and Computation* **2007,** *3*, 2011-2033.

38. Marenich, A.; Jerome, S.; Cramer, C.; Truhlar, D., Charge model 5: an extension of hirshfeld population analysis for the accurate description of molecular interactions in gaseous and condensed phases. *Journal of Chemical Theory and Computation* **2012,** *8*, 527-541.

39. Dodda, L.; Vilseck, J.; Tirado-Rives, J.; Jorgensen, W., 1.14*CM1A-LBCC: Localized Bond-Charge Corrected CM1A charges for condensed-phase simulations. *The Journal of Physical Chemistry B* **2017,** *121* (15), 3864-3870.

40. Keasler, S.; Charan, S.; Wick, C.; Economou, I.; Siepmann, J., Transferable Potentials for Phase Equilibria-United Atom description of five- and six-membered cyclic alkanes and ethers. *Journal of Physical Chemisty B* **2012,** *116*, 11234-11246.

41. Abraham, A.; Hess, B.; Van Der Spoel, M.; Lindahl, E.; and the GROMACS development team, *GROMACS User Manual version 2016*. 2016.

42. Roja, K.; Masad, E., Imfluence of chemical constituents of asphalt binders on their rheological properties. *Journal of the Transprotation Research Board* **2019,** 2673 (6).

43. Martin, M., MCCCS Towhee: a tool for Monte Carlo molecular simulation. *Molecular Simulation* **2013,** *39* (14-15), 1212-1222.

44. Park, S. J.; Seo, M. K., *Interface science and composites*. First ed.; Academic Press: 2011.

45. Zherebtsov, S.; Semenova, I.; Garbacz, H.; Motyka, M., *Nanocrystalline titanium*. Elsevier: 2019.

46. Ebnesajjad, S., Properties of tetrafluoroethylene homopolymers. In *Fluoroplastics*, Second ed.; Elsevier: 2015; Vol. 1.

47. Theodorou, D.; Suter, U., Atomistic modeling of mechanical properties of polymeric glasses. *Macromolecules* **1986,** *19*, 139-154.

48. Skountzos, E.; Anastassiou, A.; Mavrantzas, V.; Theodorou, D., Determination of the mechanical properties of a poly(methyl methacrylate) nanocomposite with functionalized graphene sheets through detailed atomistic simulations. *Macromolecules* **2014,** *47* (22), 8072-8089.

49. Israelachvili, J., Adhesion and wetting phenomena. In *Intermolecular and Surface Forces*, Third ed.; American Press: 2011; pp 415-467.

50. Xiao, S.; Edwards, S.; Grater, F., A new transferable forcefield for simulating the mechanics of $CaCO_3$ crystals. *The Journal of Physical Chemistry C* **2011,** *115*, 9.

51. Cygan, R.; Liang, J. J.; Kalinichev, A., Molecular models of hydroxides, oxyhydroxide, and clay phases and the development of a general force field. *Journal of Physical Chemistry B* **2004,** *108*, 12.

52. Jorgensen, W.; Chandrasekhar, J.; Madura, J.; Impey, R.; Klein, M., Comparison of simple potential functions for simulating liquid water. *The Journal of Chemical Physics* **1983,** *79*, 926-935.

53. Berendsen, H.; Postma, J.; Van Gunsteren, W.; Hermans, J., Interaction models for water in relation to protein hydration. In *Intermolecular Forces*, Pullman, B., Ed. Springer, Dordrecht: 1981; Vol. 14.

54. Compton, D.; Montero, S.; Murphy, W., Low-frequency Raman spectrum and asymmetric potential function for internal rotation of gaseous n-butane. *Journal of Physical Chemistry* **1980,** *84* (26), 3587-3591.

55. Wess, J.; Olsen, L.; Sweeney, M. H. *Asphalt (bitumen)*; 2005.

56. Pan, J.; Hossain, M.; Tarefder, R., Temperature and moisture impacts on asphalt before and after oxidative aging using molecular dynamics simulations. *Nanomechanics and Micromechanics* **2017,** *7* (4), 10.

57. Fazelabdolabadi, B.; Alizadeh-Mojarad, A., A molecular dynamics investigation into the adsorption behavior inside {001} kaolinite and {1014} calcite nano-scale channels: the case with confined hydrocarbon liquid, acid gases, and water. *Applied Nanoscience* **2017,** *7* (5), 155-165.

58. Wenk, H. R.; Bulakh, A., *Minerals - their constitution and origin*. Cambridge University Press: 2004.

59. Goumans, T.; Wander, A.; Brown, W.; Catlow, R., Structure and stability of the (001) a-quartz surface. *Physical Chemistry Chemical Physics* **2007,** (17).

60. Chen, Z.; Xie, J.; Xiao, Y.; Chen, J.; Wu, S., Characteristics of bonding behavior between basic oxygen furnace slag and asphalt binder. *Construction and Building Materials* **2014,** *64*, 60-66.

61. Zhang, J.; Apeagyei, A.; Airey, G.; Grenfell, J., Influence of aggregate mineralogical composition on water resistance of aggregate–bitumen adhesion. *International Journal of Adhesion and Adhesives* **2015,** *62*, 45-54.

62. Harris, K.; Newitt, P.; Woolf, L., Temperature and density dependence of the viscosity of cyclopentane. *Journal of Chemical & Engineering Data* **2004,** *49* (1), 138-142.

63. Maloney, J., *Perry's Chemical Engineers' Handbook*. 8 ed.; The McGraw-Hill Companies, Inc.: 2008.

64. Kao, Y. C.; Tu, C. H., Densities, viscosities, refractive indices, and surface tensions for binary and ternary mixtures of 2-propanol, tetrahydropyran, and 2,2,4-trimethylpentane. *The Journal of Chemical Thermodynamics* **2011,** *43* (2), 216-226.

65. Das, A.; Frenkel, M.; Gadalla, N.; Kudchadker, S.; Marsh, K.; Rodgers, A.; Wilhoit, R., Thermodynamic and thermophysical properties of organic nitrogen compounds. part II. 1- and 2-butanamine, 2-methyl-1-propanamine, 2-methyl-2-propanamine, pyrrole, 1-,2-, and 3-methylpyrrole, pyridine, 2-,3-, and 4-methylpyridine, pyrrolidine, piperidine, indole, quinoline, isoquinoline, acridine, carbazole, phenanthridine, 1- and 2-naphthalenamine, and 9-methylcarbazole. *Journal of Physical and Chemical Reference Data* **1993,** *22* (3), 659-782.

66. Rai, N.; Siepmann, J., Transferable Potentials for Phase Equilibria. 9. explicit hydrogen description of benzene and five-membered and six-membered heterocyclic aromatic compounds. *The Journal of Physical Chemistry B* **2007,** *111* (36), 10790-10799.

67. Rai, N.; Siepmann, J., Transferable Potentials for Phase Equilibria. 10. explicit-hydrogen description of substituted benzenes and polycyclic aromatic compounds. *The Journal of Physical Chemistry B* **2013,** *117* (1), 273-288.

APPENDIX A[1]

Table 10: Nonbonded parameters for the OPLS-AA force field[6]

Atom Type	Description	Molecular Weight (u)	σ (nm)	ε (kJ/mol)
opls-SSA	aromatic S	36.0600	0.360	1.485320
opls-OOA	aromatic O	15.9990	0.312	0.711280
opls-OOO	aliphatic O	15.9990	0.290	0.585760
opls-NNA	aromatic N	14.0070	0.325	0.711280
opls-CCN	aromatic C	12.0110	0.375	0.439320
opls-CCA	aromatic C	12.0110	0.355	0.292880
opls-CAA	aromatic C	12.0110	0.350	0.347200
opls-CCC	aliphatic C	12.0110	0.350	0.276144
opls-HHH	aliphatic H	1.0080	0.250	0.125520
opls-HHA	aromatic H	1.0080	0.242	0.125520
opls-HHO	H attached to O	1.0080	0.000	0.000000
opls-HHN	H attached to N	1.0080	0.000	0.000000

Table 11: Nonbonded parameters for the CLAYFF force field[51]

Atom Type	Description	Molecular Weight (u)	Charge (e)	R_0 (Å)	D_0 (kcal/mol)
st	tetrahedral silicon	28.0855	2.1000	3.7064	1.8405×10^{-6}
ob	bridging oxygen	15.9990	-1.0500	3.5532	0.1554
oh	hydroxyl oxygen	15.9990	-0.9500	3.5532	0.1554
ho	hydroxyl hydrogen	1.0080	0.4250	0.0000	0.0000

[1] All bonded parameters can be found in the literature papers mentioned in Appendix A

Table 12: Nonbonded parameters for TIP3P force field[52]

Atom Type	Description	Molecular Weight (u)	Charge (e)	C_{12} (kJ/mol.nm^{12})	C_6 (kJ/mol.nm^6)
O_w	water oxygen	15.9990	-0.830	2.44×10^{-6}	2.49×10^{-3}
H_w	water hydrogen	1.0080	0.415	0	0

Table 13: Atomwise nonbonded parameters for Xiao et.al. force field[50]

Atom Type	Description	Molecular Weight (u)	Charge (e)	C_{12} (kJ/mol.nm^{12})	C_6 (kJ/mol.nm^6)
Ca	calcium	40.0780	1.668	2.52×10^{-7}	1.42×10^{-3}
C_m	calcite carbon	12.0110	0.999	1.44×10^{-5}	4.61×10^{-3}
O_m	calcite oxygen	15.9990	-0.889	1.77×10^{-6}	2.03×10^{-3}

Table 14: Pairwise nonbonded parameters for the Xiao et.al. force field[50]

Atom Type 1	Atom Type 2	C_{12} (kJ/mol.nm^{12})	C_6 (kJ/mol.nm^6)
Ca	O_m	9.49×10^{-7}	0
C_m	C_m	4.61×10^{-6}	1.43×10^{-2}
C_m	O_m	9.04×10^{-10}	3.08×10^{-4}
O_m	O_m	5.94×10^{-7}	5.21×10^{-5}
Ca	O_w	8.85×10^{-7}	2.00×10^{-3}
C_m	O_w	5.91×10^{-6}	3.39×10^{-3}
O_m	O_w	2.07×10^{-6}	2.25×10^{-3}
O_m	H_w	7.98×10^{-9}	9.65×10^{-7}

APPENDIX B

Table 15: Density data for linear and branched alkanes

	pentane					
	P (bar)	2				
	T (K)	298.15	308.15	318.15	328.15	NIST
	Exp. (kg/m3)	620.96	610.64	600.64	590.02	
Simu. (kg/m3)	OPLS-AA	617.48	605.59	592.48	579.25	This
	TraPPE	623.28	612.96	602.55	591.75	Work
Error (%)	OPLS-AA	0.56%	0.83%	1.36%	1.83%	
	TraPPE	0.37%	0.38%	0.32%	0.29%	

	2,methylpentane					
	P (bar)	1.013				
	T (K)	298.15	308.15	318.15	328.15	NIST
	Exp. (kg/m3)	648.6	639.33	629.88	620.21	
Simu. (kg/m3)	OPLS-AA	658.72	647.43	636.2	624.94	This
	TraPPE	654.08	644.49	634.47	624.66	Work
Error (%)	OPLS-AA	1.56%	1.27%	1.00%	0.76%	
	TraPPE	0.84%	0.81%	0.73%	0.72%	

	dodecane					
	P (bar)	1.013				
	T (K)	298.15	308.15	318.15	328.15	NIST
	Exp. (kg/m3)	745.73	738.34	730.95	723.56	
Simu. (kg/m3)	OPLS-AA	749.05	740.35	730.56	722.87	This
	TraPPE	755.03	747.33	740.45	732.9	Work
Error (%)	OPLS-AA	0.45%	0.27%	0.05%	0.10%	
	TraPPE	1.25%	1.22%	1.30%	1.29%	

Table 16: Density data for cyclic alkanes

	cyclopentane					
	P (bar)	1.013				PAPER[62]
	T (K)	283.15	288.15	293.15	298.15	
	Exp. (kg/m3)	754.76	749.85	744.9	739.92	
Simu. (kg/m3)	OPLS-AA	740.05	735.16	728.66	723.16	This Work
	TraPPE	729.77	721.05	712.64	706	
Error (%)	OPLS-AA	1.95%	1.96%	2.18%	2.27%	
	TraPPE	3.31%	3.84%	4.33%	4.58%	

	cyclohexane					
	P (bar)	1.013				NIST
	T (K)	298.15	308.15	318.15	328.15	
	Exp. (kg/m3)	773.89	764.37	754.78	745.08	
Simu. (kg/m3)	OPLS-AA	764.32	752.92	742.73	730.15	This Work
	TraPPE	794.96	785.49	775.49	767.3	
Error (%)	OPLS-AA	1.24%	1.50%	1.60%	2.00%	
	TraPPE	2.72%	2.76%	2.74%	2.98%	

Table 17: Density data for benzene

	benzene					
	P (bar)	1.013				NIST
	T (K)	298.15	308.15	318.15	328.15	
	Exp. (kg/m3)	873.67	863.08	852.33	841.44	
Simu. (kg/m3)	OPLS-AA	905.86	895.93	883.39	871.07	This Work
	TraPPE	867.88	858.28	847.74	838.16	
Error (%)	OPLS-AA	3.68%	3.81%	3.64%	3.52%	
	TraPPE	0.66%	0.56%	0.54%	0.39%	

Table 18: Density data for naphthalene

	naphthalene					
	P (bar)	3.26	7.16	13.82	24.51	PHB[63]
	T (K)	550	600	650	700	PAPER[27]
	Exp. (kg/m3)	771	718	655	572	
Simu. (kg/m3)	OPLS-AA	829.65	771.53	704.53	609.55	This Work
	TraPPE	769	721	655	570	PAPER[27]
Error (%)	OPLS-AA	7.61%	7.46%	7.56%	6.56%	
	TraPPE	0.26%	0.42%	0.00%	0.35%	

Table 19: Density data for hetero-molecules 1

	oxane					
	P (bar)	1.013				PAPER[64]
	T (K)	293.15	303.15	313.15	323.15	
	Exp. (kg/m3)	884.27	874.07	863.76	853.46	
Simu. (kg/m3)	OPLS-AA	889.18	876.56	867.2	855.24	This Work
	TraPPE	920.16	907.78	899.83	890.43	
Error (%)	OPLS-AA	0.56%	0.28%	0.40%	0.21%	
	TraPPE	4.06%	3.86%	4.18%	4.33%	

	thiophene					
	P (bar)	2.7	7.85	18.17	30.74	PHB
	T (K)	393.15	443.15	493.15	530.15	PAPER[31]
	Exp. (kg/m3)	938.13	864.34	777.03	694.93	PHB
Simu. (kg/m3)	OPLS-AA	1012.15	945.37	874.58	812.12	This work
	TraPPE	936.52	872.92	798.41	734.36	PAPER[31]
Error (%)	OPLS-AA	7.89%	9.37%	12.55%	16.86%	
	TraPPE	0.17%	0.99%	2.75%	5.67%	

Table 20: Density data for hetero-molecules 2

	pyrrole					
	P (bar)	0.3409	2.739	13.35	31.71	PAPER[65]
	T (K)	370	440	520	580	
	Exp. (kg/m3)	899	828	730	633	
Simu. (kg/m3)	OPLS-AA	1026.93	957.99	865.1	775.12	This Work
	TraPPE	900.6	827.4	736.6	638.2	PAPER[65]
Error (%)	OPLS-AA	14.23%	15.70%	18.51%	22.45%	
	TraPPE	0.18%	0.07%	0.90%	0.82%	

	pyridine					
	P (bar)	1.33	6.54	16.42	33.36	PAPER[65]
	T (K)	398.1	468.1	523.1	575.1	PAPER[66]
	Exp. (kg/m3)	873.47	792.47	717.61	622.07	PAPER[65]
Simu. (kg/m3)	OPLS-AA	931.39	853.21	789.02	716.17	This Work
	TraPPE	874.8	784.3	709.1	594.1	PAPER[66]
Error (%)	OPLS-AA	6.63%	7.66%	9.95%	15.13%	
	TraPPE	0.15%	1.03%	1.19%	4.50%	

	phenol					
	P (bar)	1.92	6.61	17.23	34.12	PHB
	T (K)	480	540	600	650	PAPER[67]
	Exp. (kg/m3)	899.85	830.67	747.94	655.83	PHB
Simu. (kg/m3)	OPLS-AA	928.55	853.86	760.28	664.21	This Work
	TraPPE	888.55	813.26	720.21	613.6	PAPER[67]
Error (%)	OPLS-AA	3.19%	2.79%	1.65%	1.28%	
	TraPPE	1.26%	2.10%	3.71%	6.44%	